# Session 3P5
# Electromagnetic Modeling and Inversion and Applications 3

# New Stochastic AGLID EM Modeling and Inversion

**J. Li**, **G. Xie**, **L. Xie**, **and F. Xie**
GL Geophysical Laboratory, USA

**Abstract**—The AGILD modeling and inversion have been published in PIERS2005 in Hangzhou. The new 2.5D AGILD and new GL electromagnetic (EM) modeling and inversion are publishing in PIERS2006 in Cambridge of USA. We have proposed the stochastic SGILD modeling and inversion in nano-physics and geophysics using magnetic field equations in 1999 and 2002. In this paper, we present a new stochastic AGILD (SAGILD) EM modeling and inversion and software. We propose a new EM integral equation on the strip domain. Based on the strip integral equation, we propose new stochastic EM field strip integral equations for mean, covariance, and second order mean EM field and parameters. These stochastic EM moments strip integral equations are employed on the boundary strip domain. In the cylindrical and spherical coordinate system, the strip domain includes the boundary and pole strip involving pole $\rho = 0$ or $r = 0$, North Pole $\theta = 0$ and South Pole $\theta = \pi$. In the remainder internal domain, we use stochastic moments Galerkin equations. We coupled these equations to construct 3D and 2.5D SAGILD modeling algorithms. By decomposing the variance of the parameter mean, $\delta < \sigma + i\omega\varepsilon >= \delta < \sigma + i\omega\varepsilon >_0 + \delta < \sigma + i\omega\varepsilon >_2$, $\delta < \mu >= \delta < \mu >_0 + \delta < \mu >_2$, we derive the new stochastic EM parameters increment moment strip integral equation on the strip sub domain for isotropic or anisotropic random materials. We used the equation pair of EM parameter stochastic integral equations on the strip sub domain and EM parameter stochastic Galerkin equation in remainder sub domain to construct the SAGILD inversion. The SAGILD modeling and inversion have widely applications in the Earth, Sun, and Luna space EM field exploration, nanometer material and material sciences, geophysical and Earthquake exploration, MT, MAIL, VEMP, weather radar imaging, medical MRI and X-ray imaging, and environmental engineering, EM stirring in steel and metal continuous casting, seismic, and finances.

## 1. Introduction

We have proposed the stochastic SGILD EM modeling and inversion in geophysics and nano-physics using magnetic field equations in 1999 [1] and 2002 [2]. A new GL method and its advantages for resolving historical difficulties will be published in PIERS2006 in Cambridge of USA [3]. The AGILD modeling and inversion has been published in PIERS2005 in Hangzhou [4], and the 2.5D AGILD modeling and inversion will be published in PIERS2006 in Cambridge USA [5]. In this paper, we propose a new SAGILD EM modeling and inversion. First, we propose a new EM integral equation on the boundary strip for rectangle coordinate or boundary pole strip domain for cylindrical and spherical coordinate. Next, we propose new stochastic EM field integral equations for mean, covariance field and parameters, and second order mean field and parameter. These stochastic EM moment strip integral equations are employed on the strip domain. In the cylindrical and spherical coordinate system, the strip domain includes the boundary and pole strip domain with poles $\rho = 0$ or $r = 0$, North Pole $\theta = 0$ and South Pole $\theta = \pi$. In the remainder internal domain, we use stochastic moments EM Galerkin equations. We couple these equations to construct the 3D/2.5D SAGILD modeling. By decomposing the variance of the mean of the parameters, $\delta < \mu >= \delta < \mu >_0 + \delta < \mu >_2$, $\delta < \sigma + i\omega\varepsilon >= \delta < \sigma + i\omega\varepsilon >_0 + \delta < \sigma + i\omega\varepsilon >_2$. We derive the stochastic EM parameters moment strip integral equations on the strip sub domain for isotropic or anisotropic materials. These new parameter integral equations are described in our internal report in detail [6]. We use the EM parameter stochastic integral equations on the strip sub domain and EM parameter stochastic Galerkin equation in remainder sub domain to construct the SAGILD inversion. In the cylindrical and spherical coordinate, the strip domain contains the poles for resolving the coordinate singularity difficulty.

The SAGILD modeling and inversion have widely applications in the Earth, Sun, and Luna space EM field exploration, nanometer material and material sciences, geophysical and Earthquake exploration, MT, MAIL, VEMP, weather radar imaging, medical MRI and X-ray imaging, and environmental engineering, and EMS stirring in metal casting, random flows, and finances. The new SAGILD modeling and inversion have advantages over existing random method. The SAGILD methods have AGILD's merits and improved field and parameter moments and its confidences.

We arrange contents in this paper as follows. The introduction has been described in the section 1. In section 2, we propose a new EM strip integral equation. The new stochastic EM moment strip integral equation is presented in the section 3. The stochastic EM Garlekin equation is presented in the section 4. In section

5, we propose the stochastic EM modeling. The stochastic EM inversion is presented in the section 6. The applications are described in the section 7. In section 8, we describe conclusions.

## 2. The New EM Strip Integral Equation

We have proposed EM integral equations in the paper [3], in which, our EM integral equations are

$$\begin{bmatrix} E(r) \\ H(r) \end{bmatrix} = \begin{bmatrix} E_b(r) \\ H_b(r) \end{bmatrix} + \int_{\Omega} \begin{bmatrix} E_b^J(r',r) & H_b^J(r',r) \\ E_b^M(r',r) & H_b^M(r',r) \end{bmatrix} [D] \begin{bmatrix} E(r') \\ H(r') \end{bmatrix} dr', \tag{1}$$

$$\begin{bmatrix} E(r) \\ H(r) \end{bmatrix} = \begin{bmatrix} E_b(r) \\ H_b(r) \end{bmatrix} + \int_{\Omega} \begin{bmatrix} E^J(r',r) & H^J(r',r) \\ E^M(r',r) & H^M(r',r) \end{bmatrix} [D] \begin{bmatrix} E_b(r') \\ H_b(r') \end{bmatrix} dr'. \tag{2}$$

That is available for the rectangle, cylindrical, and spherical coordinate systems. In our paper [5], we proposed the 2.5D EM differential integral equation in the cylindrical coordinate system. In this section, we propose the new EM strip integral equations on the strip domain in rectangle or strip pole domain in the cylindrical and spherical coordinate for resolving coordinate singularity.

$$\begin{bmatrix} E(r) \\ H(r) \end{bmatrix} = \begin{bmatrix} E_b(r) \\ H_b(r) \end{bmatrix} + \int_{\Omega_s} \begin{bmatrix} E_b^J(r',r) & H_b^J(r',r) \\ E_b^M(r',r) & H_b^M(r',r) \end{bmatrix} [D] \begin{bmatrix} E(r') \\ H(r') \end{bmatrix} dr' - \int_{\partial\Omega s-} \begin{bmatrix} H_b^J(r',r) & E_b^J(r',r) \\ H_b^M(r',r) & E_b^M(r',r) \end{bmatrix} \times \begin{bmatrix} E(r') \\ H(r') \end{bmatrix} d\vec{S}r', \tag{3}$$

$$\begin{bmatrix} E(r) \\ H(r) \end{bmatrix} = \begin{bmatrix} E_b(r) \\ H_b(r) \end{bmatrix} + \int_{\Omega_s} \begin{bmatrix} E^J(r',r) & H^J(r',r) \\ E^M(r',r) & H^M(r',r) \end{bmatrix} [D] \begin{bmatrix} E_b(r') \\ H_b(r') \end{bmatrix} dr' - \int_{\partial\Omega s-} \begin{bmatrix} H^J(r',r) & E^J(r',r) \\ H^M(r',r) & E^M(r',r) \end{bmatrix} \times \begin{bmatrix} E_b(r') \\ H_b(r') \end{bmatrix} d\vec{S}r'. \tag{4}$$

The EM strip integral equations are dual equation each other. The equations (3) and (4) are available for the rectangle, cylindrical, and spherical coordinate systems. In the rectangle coordinate $r = (x, y, z)$, $E = (E_x, E_y, E_z)$, $dr = dxdydz$, in the cylindrical coordinate $E = (E_\rho, E_\theta, E_z)$, $dr = \rho d\rho d\theta dz$, in spherical coordinate, $dr = r^2 \sin\theta dr d\theta d\phi$, $dS = r^2 d\theta d\phi \boldsymbol{r} + r\sin\theta d\phi dr\theta + r dr d\theta \boldsymbol{\phi}$, $E = (E_r, E_\theta, E_\phi)$. For the isotropic materials, the material matrix [D] is the $6\times 6$ diagonal matrix with variance of the conductivity and permittivity, $(\sigma - \sigma_b) + i\omega(\varepsilon - \varepsilon_b)$, and the magnetic permeability, $\mu - \mu_b$. For anisotropic materials, the matrix [D] is a full matrix with variance of the anisotropic materials. Obviously, the EM strip integral equations have no any coordinate singularity.

## 3. The Stochastic EM Field Moment Strip Integral Equations

Upon substituting the decomposition of the EM field,

$$\begin{bmatrix} E(r) \\ H(r) \end{bmatrix} = \begin{bmatrix} E(r) \\ H(r) \end{bmatrix}_0 + \begin{bmatrix} E(r) \\ H(r) \end{bmatrix}_1 + \begin{bmatrix} E(r) \\ H(r) \end{bmatrix}_2, \tag{5}$$

and the decomposition of the material matrix

$$[D] =< [D] > + [D]_s, \tag{6}$$

into the equation (3), we propose the stochastic EM moment strip integral equations,

$$\begin{bmatrix} E(r) \\ H(r) \end{bmatrix}_0 = \begin{bmatrix} E_b(r_s) \\ H_b(r) \end{bmatrix} + \int_{\Omega} \begin{bmatrix} E_b^J(r',r) & H_b^J(r',r) \\ E_b^M(r',r) & H_b^M(r',r) \end{bmatrix} \langle\!\langle [D] \rangle\!\rangle \begin{bmatrix} E(r') \\ H(r') \end{bmatrix}_0 dr' - \int_{\partial\Omega-} \begin{bmatrix} H_b^J(r',r) & E_b^J(r',r) \\ H_b^M(r',r) & E_b^M(r',r) \end{bmatrix} \times \begin{bmatrix} E(r') \\ H(r') \end{bmatrix}_0 d\vec{S}, \tag{7}$$

and the following three stochastic EM field moment strip integral equations. Let *AGILDMI* to be the stochastic EM field moment integral operator

$$\begin{aligned} AGILDMI\left( \begin{bmatrix} C_{\sigma E} & C_{\mu E} \\ C_{\sigma H} & C_{\mu H} \end{bmatrix}, \begin{bmatrix} C_{\sigma\sigma} & C_{\mu\sigma} \\ C_{\sigma\mu} & C_{\mu\mu} \end{bmatrix}, \begin{bmatrix} E_0 \\ H_0 \end{bmatrix} \right) &= \begin{bmatrix} C_{\sigma E} & C_{\mu E} \\ C_{\sigma H} & C_{\mu H} \end{bmatrix}(r) - \int_{\Omega} \begin{bmatrix} E_b^J(r',r) & H_b^J(r',r) \\ E_b^M(r',r) & H_b^M(r',r) \end{bmatrix} \langle\!\langle [D] \rangle\!\rangle \begin{bmatrix} C_{\sigma E} & C_{\mu E} \\ C_{\sigma H} & C_{\mu H} \end{bmatrix}(r') dr' \\ - \int_{\Omega} \begin{bmatrix} E_b^J(r',r) H_b^J(r',r) \\ E_b^M(r',r) H_b^M(r',r) \end{bmatrix} \begin{bmatrix} E_0 C_{\sigma\sigma} E_0 C_{\mu\sigma} \\ H_0 C_{\sigma\mu} H_0 C_{\mu\mu} \end{bmatrix}(r') dr' &+ \int_{\partial\Omega-} \begin{bmatrix} H_b^J(r',r) E_b^J(r',r) \\ H_b^M(r',r) E_b^M(r',r) \end{bmatrix} \times \left( \begin{bmatrix} C_{\sigma E} C_{\mu E} \\ C_{\sigma H} C_{\mu H} \end{bmatrix} + \begin{bmatrix} E_0 C_{\sigma\sigma} E_0 C_{\mu\sigma} \\ H_0 C_{\sigma\mu} H_0 C_{\mu\mu} \end{bmatrix} \right)(r') d\vec{S}, \end{aligned} \tag{8}$$

$$AGILDMI\left(\begin{bmatrix} C_{\sigma E} & C_{\mu E} \\ C_{\sigma H} & C_{\mu H} \end{bmatrix}, \begin{bmatrix} C_{\sigma\sigma} & C_{\mu\sigma} \\ C_{\sigma\mu} & C_{\mu\mu} \end{bmatrix}, \begin{bmatrix} E_0 \\ H_0 \end{bmatrix}\right) = 0, \tag{9}$$

$$AGILDMI\left(\begin{bmatrix} C_{EE} C_{EH} \\ C_{EH} C_{HH} \end{bmatrix}, \begin{bmatrix} C_{\sigma E} C_{\mu E} \\ C_{\sigma H} C_{\mu H} \end{bmatrix}, \begin{bmatrix} E_0 \\ H_0 \end{bmatrix}\right) = 0, \tag{10}$$

$$\left\langle \begin{bmatrix} E \\ H \end{bmatrix}_2 \right\rangle = \int_\Omega \begin{bmatrix} E_b^J(r',r) & H_b^J(r',r) \\ E_b^M(r',r) & H_b^M(r',r) \end{bmatrix} \langle [D] \rangle \left\langle \begin{bmatrix} E(r') \\ H(r') \end{bmatrix}_2 \right\rangle dr - \int_{\partial\Omega-} \begin{bmatrix} H_b^J(r',r) & E_b^J(r',r) \\ H_b^M(r',r) & E_b^M(r',r) \end{bmatrix} \times \left\langle \begin{bmatrix} E(r') \\ H(r') \end{bmatrix}_2 \right\rangle d\vec{S}(r')$$
$$+ \int_\Omega \begin{bmatrix} E_b^J(r',r) & H_b^J(r',r) \\ E_b^M(r',r) & H_b^M(r',r) \end{bmatrix} \begin{bmatrix} \hat{C}_{\sigma E} \\ \hat{C}_{\mu H} \end{bmatrix} dr - \int_{\partial\Omega-} \begin{bmatrix} H_b^J(r',r) & E_b^J(r',r) \\ H_b^M(r',r) & E_b^M(r',r) \end{bmatrix} \times \begin{bmatrix} \hat{C}_{\sigma E} \\ \hat{C}_{\mu H} \end{bmatrix} d\vec{S}(r'), \tag{11}$$

## 4. The Stochastic EM Field Garlekin Equation

We propose the EM Garlekin equation in the rectangle, cylindrical, and spherical coordinate.

$$\oint_{\partial\Omega} [E\ H]_0 \times \phi I d\vec{S} - \int_\Omega [E\ H]_0 \nabla \times \phi I d\Omega = \int_\Omega [E\ H]_0 \begin{bmatrix} 0 & \langle\sigma\rangle \\ -i\omega\langle\mu\rangle & 0 \end{bmatrix} \phi I d\Omega + \int_\Omega [J_s\ M_s] \begin{bmatrix} 0 & 1 \\ -i\omega\langle\mu\rangle & 0 \end{bmatrix} \phi I d\Omega, \tag{12}$$

$$AGILDMG\left(\begin{bmatrix} C_{\sigma E} & C_{\mu E} \\ C_{\sigma H} & C_{\mu H} \end{bmatrix}, \begin{bmatrix} C_{\sigma\sigma} & C_{\mu\sigma} \\ C_{\sigma\mu} & C_{\mu\mu} \end{bmatrix}, \begin{bmatrix} E_0 \\ H_0 \end{bmatrix}\right) = \oint_{\partial\Omega} \begin{bmatrix} C_{\sigma E} & C_{\mu E} \\ C_{\sigma H} & C_{\mu H} \end{bmatrix} \times \phi I d\vec{S} - \int_\Omega \begin{bmatrix} C_{\sigma E} & C_{\mu E} \\ C_{\sigma H} & C_{\mu H} \end{bmatrix} \nabla \times \phi I d\Omega$$
$$- \int_\Omega \begin{bmatrix} 0 & \langle\sigma\rangle \\ -i\omega\langle\mu\rangle & 0 \end{bmatrix} \begin{bmatrix} C_{\sigma E} C_{\mu E} \\ C_{\sigma H} C_{\mu H} \end{bmatrix} \phi I d\Omega - \int_\Omega \begin{bmatrix} E_0 C_{\sigma\sigma} & E_0 C_{\mu\sigma} \\ H_0 C_{\sigma\mu} & H_0 C_{\mu\mu} \end{bmatrix} \phi I d\Omega, \tag{13}$$

$$AGILDMG\left(\begin{bmatrix} C_{\sigma E} & C_{\mu E} \\ C_{\sigma H} & C_{\mu H} \end{bmatrix}, \begin{bmatrix} C_{\sigma\sigma} & C_{\mu\sigma} \\ C_{\sigma\mu} & C_{\mu\mu} \end{bmatrix}, \begin{bmatrix} E_0 \\ H_0 \end{bmatrix}\right) = 0, \tag{14}$$

$$AGILDMG\left(\begin{bmatrix} C_{EE} C_{EH} \\ C_{EH} C_{HH} \end{bmatrix}, \begin{bmatrix} C_{\sigma E} C_{\mu E} \\ C_{\sigma H} C_{\mu H} \end{bmatrix}, \begin{bmatrix} E_0 \\ H_0 \end{bmatrix}\right) = 0, \tag{15}$$

$$\oint_{\partial\Omega} \langle [E\ H]_2 \rangle \times \phi I d\vec{S} - \int_\Omega \langle [E\ H]_2 \rangle \nabla \times \phi I d\Omega = \int_\Omega \langle [E\ H]_2 \rangle \begin{bmatrix} 0 & \langle\sigma\rangle \\ -i\omega\langle\mu\rangle & 0 \end{bmatrix} \phi I d\Omega + \int_\Omega \begin{bmatrix} \hat{C}_{\sigma E} & \hat{C}_{\mu H} \end{bmatrix} \begin{bmatrix} 0 & 1 \\ -i\omega\langle\mu\rangle & 0 \end{bmatrix} \phi I d\Omega, \tag{16}$$

The above stochastic EM moment strip integral equations are available for isotropic materials. For anisotropic materials, the stochastic EM moment strip integral equations can be derived similarly. The $[C_{\sigma E}]$ is covariance moment matrix, $C_{\sigma E} =< E(r)\sigma(\Re) >, <, >$ is assemble mean, other covariance terms are defined similarly. $\hat{C}_{IJ} = \langle I(r)J(\Re)\rangle|_{r=\Re} I = \sigma,\ J = E,\ H$, $[C_{IJ}] = [< I(r), J(\Re) >]$, $I,\ J = \sigma,\ \mu$.

## 5. The New Stochastic SAGILD EM Modeling

### 5.1 The AGILD Pair of the Strip Integral Equation and the Garlekin Equation

In our AGILD modeling [4], we couple the strip integral equation or differential integral equation in the strip domain and the Garlekin equation in the remainder internal domain for solving EM field. We call the strip integral equation and Garlekin equation to be AGILDM pair. In the section 4, the stochastic EM moment strip integral equations (7–11) and EM moment Garlekin equation (12–16) are used to form AGILD pair AGILDM{7,12}; AGILDM{9,14}, AGILDM{10,15}, AGILDM{11,16}.

### 5.2 The New SAGILD EM Modeling

We propose the SAGILD EM modeling as following five steps,

(M.1) use AGILD modeling to solve the pair equations AGILDM{7,12} for $< [E(r), H(r)] >_0$;
(M.2) use AGILD to solve the pair equations AGILDM{9,14} for $[C_{IJ}(r))]$, $I = \sigma,\ \mu,\ J = E, H$;
(M.3) use AGILD to solve the pair equations AGILDM{10,15} for $[C_{IJ}(r))]$, $I = E, H,\ J = E, H$;
(M.4) use AGILD to solve the pair equations AGILDM{11,16} for $< [E(r), H(r)] >_2$;

(M.5) to update $< [E(r), H(r)] >_{=} < [E(r), H(r)] >_0 + < [E(r), H(r)] >_2$.

## 6. The New Stochastic SAGILD EM Inversion

### 6.1 The EM Parameter Variation Moment Strip Integral Equations

$$\delta \begin{bmatrix} E \\ H \end{bmatrix}_0 (r_d) = \int_{\Omega} \begin{bmatrix} E_b^J(r',r) & H_b^J(r',r) \\ E_b^M(r',r) & H_b^M(r',r) \end{bmatrix} \delta \langle [D]_0 \rangle \begin{bmatrix} E \\ H \end{bmatrix}_0 (r') dr' - \int_{\partial\Omega -} \begin{bmatrix} H_b^J(r',r) & E_b^J(r',r) \\ H_b^M(r',r) & E_b^M(r',r) \end{bmatrix} \times \delta \begin{bmatrix} E \\ H \end{bmatrix}_0 (r') d\vec{S}, \tag{17}$$

$$AGILDII\left(\delta \begin{bmatrix} C_{\sigma E} & C_{\mu E} \\ C_{\sigma H} & C_{\mu H} \end{bmatrix}, \delta \begin{bmatrix} C_{EE} & C_{EH} \\ C_{EH} & C_{HH} \end{bmatrix}, \delta[D_0]\right) = \delta \begin{bmatrix} C_{EE} & C_{EH} \\ C_{EH} & C_{HH} \end{bmatrix} (r_d) - \int_{\Omega} \begin{bmatrix} E_b^J(r',r) & H_b^J(r',r) \\ E_b^M(r',r) & H_b^M(r',r) \end{bmatrix} \delta \begin{bmatrix} C_{\sigma E} & C_{\mu E} \\ C_{\sigma H} & C_{\mu H} \end{bmatrix} \begin{bmatrix} E \\ H \end{bmatrix}_0 dr' + \int_{\partial\Omega -} \begin{bmatrix} H_b^J(r',r) & E_b^J(r',r) \\ H_b^M(r',r) & E_b^M(r',r) \end{bmatrix} \times \delta \begin{bmatrix} C_{EE} & C_{EH} \\ C_{EH} & C_{HH} \end{bmatrix} d\vec{S}, \tag{18}$$

$$AGILDII\left(\delta \begin{bmatrix} C_{\sigma E} & C_{\mu E} \\ C_{\sigma H} & C_{\mu H} \end{bmatrix}, \delta \begin{bmatrix} C_{EE} & C_{EH} \\ C_{EH} & C_{HH} \end{bmatrix}_d, \delta[D_0]\right) = 0, \tag{19}$$

$$AGILDII\left(\delta \begin{bmatrix} C_{\sigma\sigma} & C_{\mu\sigma} \\ C_{\sigma\mu} & C_{\mu\mu} \end{bmatrix}, \delta \begin{bmatrix} C_{\sigma E} & C_{\mu E} \\ C_{\sigma H} & C_{\mu H} \end{bmatrix}_d, \delta[D_0]\right) = 0, \tag{20}$$

$$\delta \left\langle \begin{bmatrix} E \\ H \end{bmatrix}_2 \right\rangle (r_d) = \int_{\Omega} \begin{bmatrix} E_b^J(r',r) & H_b^J(r',r) \\ E_b^M(r',r) & H_b^M(r',r) \end{bmatrix} \delta \langle [D]_2 \rangle \begin{bmatrix} E \\ H \end{bmatrix}_0 (r') dr' - \int_{\partial\Omega -} \begin{bmatrix} H_b^J(r',r) & E_b^J(r',r) \\ H_b^M(r',r) & E_b^M(r',r) \end{bmatrix} \times \delta \left( \begin{bmatrix} E \\ H \end{bmatrix}_0 + \left\langle \begin{bmatrix} E \\ H \end{bmatrix} \right\rangle_2 \right) d\vec{S} + \int_{\Omega} \begin{bmatrix} E_b^J(r',r) & H_b^J(r',r) \\ E_b^M(r',r) & H_b^M(r',r) \end{bmatrix} \delta \langle [D]_0 \rangle \left\langle \begin{bmatrix} E \\ H \end{bmatrix}_2 \right\rangle (r') dr' + \int_{\Omega} \begin{bmatrix} E_b^J(r',r) & H_b^J(r',r) \\ E_b^M(r',r) & H_b^M(r',r) \end{bmatrix} \delta \begin{bmatrix} \hat{C}_{\sigma E} \\ \hat{C}_{\mu H} \end{bmatrix} (r') dr'. \tag{21}$$

### 6.2 The EM Parameter Variation Moment Garlekin Equations

$$\oint_{\partial\Omega} \delta[E\ H]_0 \times \phi I d\vec{S} - \int_{\Omega} \delta[E\ H]_0 \nabla \times \phi I d\Omega = \int_{\Omega} [E\ H]_0 \delta[D]_0 \phi I d\Omega + \int_{\Omega} [J_s\ M_s] \delta[D]_0 \phi I d\Omega, \tag{22}$$

$$AGILDGI\left(\delta \begin{bmatrix} C_{\sigma E} & C_{\mu E} \\ C_{\sigma H} & C_{\mu H} \end{bmatrix}, \delta \begin{bmatrix} C_{EE} & C_{EH} \\ C_{EH} & C_{HH} \end{bmatrix}_d, \delta[D_0]\right) = 0, \tag{23}$$

$$AGILDGI\left(\delta \begin{bmatrix} C_{\sigma\sigma} & C_{\mu\sigma} \\ C_{\sigma\mu} & C_{\mu\mu} \end{bmatrix}, \delta \begin{bmatrix} C_{\sigma E} & C_{\mu E} \\ C_{\sigma H} & C_{\mu H} \end{bmatrix}_d, \delta[D_0]\right) = 0. \tag{24}$$

$$AGILDGII\left(\delta\langle [D]_2 \rangle, \langle \delta[E,H]_2 \rangle_d, \delta\hat{C}_{DE}, \delta[D_0]\right) = 0. \tag{25}$$

### 6.3 The SAGILD EM Parameter Inversion

We propose the SAGILD EM inversion as the following six steps,
(I.1) use AGILD inversion to solve the pair equations AGILDI{17,22} for $< \delta[D]_0 >$;
(I.2) use AGILD inversion to solve the pair equations AGILDI{19,23} for $< \delta[C_{DE}(r)] >$;
(I.3) use AGILD inversion to solve the pair equations AGILDI{20,24} for $< \delta[C_{DD}(r)] >$;
(I.4) use AGILD inversion to solve the pair equations AGILDI{21,25} for $< \delta[D]_2 >$;
(I.5) to update $< \delta[D] >_{=} < \delta[D]_0 > + < \delta[D]_2 >$;
(I.6) to do iteration (I.1)–(I.5) with regularizing to find $[D]$ such that $P([D])/P(E,H)(r_d)) = max$.

## 7. Applications

Because there are random noises in the field data and parameters in the experiment and industrial measurements, it is necessary to study stochastic EM field modeling and parameter inversion. Our SAGILD modeling and inversion have AGILD's significant merits and improved field and parameter moments and its confidences

interval. Our SAGILD methods have widely applications in the Earth, Sun, and Luna space EM field exploration, nanometer and material sciences, geophysical and Earthquake exploration, MT, MAIL, VEMP, weather imaging, medical MRI and X-ray imaging, and environmental engineering, EM stirring in casting. SAGILD is used for finances, movie field, game field, seismic wave, acoustic wave, random flow filed, QEM particle wave in nano-physics and nano-biophysics and photosynthesis in anisotropic media.

## 8. Conclusions

The all integral equations and SAGILD methods in this paper are new original works. Field and synthetic random data tests show that the SAGILD method is high resolution, stable, and reasonable accurate moment modeling and inversion algorithms. It can be used to obtain the improved EM field and parameter mean with the second mean term, covariance, and standard deviations. SAGILD is very useful for estimating uncertainty and confidence interval for field and parameters. Our SAGILD software are effective tools for EM field and parameters, finances, movie field, game field, seismic, acoustic, random flow, QEM particle wave in nano-physics and biophysics and photosynthesis. Our SAGILG MCMC stochastic method and software are developing.

### REFERENCES

1. Xie, G., J. Li, and C. C. Lin, "SGILD EM modeling and inversion in geophy and nano-physics using magnetic field eqs," *Three-Dimensional Electromagnetic MGG book*, Vol. 35, 103, 2002.
2. Xie, G. and J. Li, "New parallel stochastic global integral and local differential equation modeling and inversion," *Physics D*, Vol. 133, 477–487, 1999.
3. Xie, G., F. Xie, and J. Li, "New GL method and its advantages for resolving historical difficulties," To be presented in PIERS 2006, *Proc. of PIERS2006 in Cambridge*, 2006.
4. Xie, G., J. Li, and F. Xie, "Advanced GILD EM modeling and inversion," *Proc. of PIERS2005*, Hangzhou, China, 105–109, 2005.
5. Xie, G., J. Li, and F. Xie, "2.5D AGILD electromagnetic modeling and inversion," To be presented in PIERS 2006, *Proc. of PIERS206 in Cambridge*, 2006.
6. Li, J., G. Xie, L. Xie, and F. Xie, "Stochastic AGILD EM, seismic, acoustic, random flow, and financial modeling and inversion," Report of GLGEO, GLP05005, Its copyright and patent belong to authors in GL Geophysical Laboratory, 2005.

# Advancements in Microwave Tomography of Strong Scatterers

**R. Pierri**[1], **G. Leone**[2], **and R. Solimene**[2]

[1]Seconda Università di Napoli, Italy
[2]Università Mediterranea di Reggio Calabria, Italy

The inverse scattering problem of reconstructing strong scatterers, especially metallic ones, from scattered field measured data, is one of the most important issues in microwave imaging applications.

This contribution deals with such a problem in the framework of a two-dimensional and scalar geometry and with the possible scatterers embedded in a homogenous and lossless medium. In particular, we consider both the cases of "large" objects (i.e., scatterers whose cross-section is much larger than the wavelength) and of "thin" objects (i.e., scatterers with their cross-section much smaller than the wavelength).

For large scatterers, the Kirchhoff or Physical Optics (PO) approximation is exploited, whereas unknown scatterers shape, is represented as the support of a single-layer distribution. This allows the problem be formulated as the inversion of a linear operator we tackle by means of its Truncated Singular Value Decomposition (TSVD) [1]. As well known, the PO approximation requires that the objects are non-convex, exhibit a "smooth" surface and are not interacting. Hence, it is worthy of investigating to what extent the model error, arising by objects not meeting the above requirements, affects the linear inversion scheme. In this paper we perform this investigation for three test cases. First, with the aim of pointing out the role of the radius of curvature, we consider a circular cylinder with radius smaller than the working wavelength. Second, two interacting circular cylinders are considered. Finally, a non-convex scatterer is addressed [2].

For 'thin' scatterers, we set a linear scattering model neglecting the mutual interactions between them and consider only the leading term of the low-frequency approximation of the scattered field. Furthermore, a distributional representation of the unknown is again fruitfully introduced. However since, in this case, the unknowns are the positions of the scatterers, we represent them as the support of a linear combination of Dirac pulses. Accordingly, the inversion can be still performed by a TSVD scheme. We assess the performance of this inversion scheme against the model error due to neglecting the mutual interactions [3].

As a final point, for both above cases, a thresholding procedure aiming at mitigating spurious artefacts appearing in the reconstruction owing to regularization and noise, is proposed [4].

## REFERENCES

1. Liseno, A. and R. Pierri, "Imaging perfectly conducting objects as support of induced currents: kirchhoff approximation and frequency diversity," *J. Opt. Soc. Am. A*, Vol. 19, No. 7, 1308–1319, July 2002.
2. Pierri, R., A. Liseno, R. Solimene, and F. Soldovieri, "Beyond physical optics SVD shape reconstruction of metallic cylinders," in print on *IEEE Trans. Antennas and Propagation.*
3. Pierri, R., R. Solimene, A. Liseno, and J. Romano, "Linear distribution imaging of thin metallic cylinders under mutual scattering," *IEEE Trans. Antennas and Propagation*, Vol. 53, No. 9, 3019–3029, Sep. 2005.
4. Solimene, R., A. Liseno, and R. Pierri, "A spatially varying threshold for imaging thin metallic cylinders," submitted.

# Acceleration of the 3D FDTD Algorithm in Fixed-point Arithmetic Using Reconfigurable Hardware

**W. Chen, M. Leeser, and C. Rappaport**
Northeastern University, USA

Modelling electromagnetic behavior has become a requirement in key electrical engineering tech- nologies such as cellular phones, mobile computing, lasers and photonic circuits. The Finite-Difference Time-Domain (FDTD) method, which provides a direct, time domain solution to Maxwell's Equations in differential form with relatively good accuracy and flexibility, has become a powerful method for solving a wide variety of different electromagnetics problems. The FDTD method was not widely used until the past decade when computing resources improved. Even today, the computational cost is still too high for real-time application of the FDTD method.

Much effort has been spent on software acceleration research and people have used supercomputers or parallel computer arrays to calculate the FDTD algorithm in software. However, real-time application of the FDTD algorithm needs much faster speed as well as smaller size. Although Application Specific Integrated Circuits (ASICs) provide the speed, designers hesitate to apply the FDTD algorithm to ASICs due to the high cost. Recently, as high capacity Field-Programmable Gate Arrays (FPGAs) have emerged, researchers have become interested in reconfigurable hardware implementations of the FDTD algorithm for faster calculation and real-time applications.

We present the first fixed-point 3D FDTD FPGA accelerator, which supports a wide range of materials including dispersive media. By analyzing the performance of fixed-point arithmetic in both soil-based media and human tissue media, we choose the right fixed-point representation to minimize the relative error between fixed-point and floating point results to less than 0.5%. The FPGA accelerator supports the UPML absorbing boundary conditions which have better performance in dispersive soil and human tissue media than PML boundary conditions. Finally, the FPGA design implements and supports three FDTD applications including the Ground Penetrating Radar buried object detection model, the microwave breast cancer detection model and the spiral antenna model. Based on these three applications, our FPGA design can support a wide range of FDTD applications.

Implementation of the FDTD in hardware greatly increases its computational speed. The speedup is due to three major factors: custom memory interface design, pipelining and parallelism. The FDTD method is a data intensive algorithm; the bottleneck of the hardware design is its memory interface. With the limited bandwidth between FPGA and data memories, a carefully designed custom memory interface will fully utilize the memory bandwidth and greatly improve the design performance. Also, by considering the tradeoff between speedup and chip areas, we implement as much pipeline and parallelism as possible to speed up the design.

The 3D FDTD design is implemented on an AnnapolisWildStar$^{TM}$-II Pro/PCI FPGA board which represents the leading technology in FPGA COTS (commercial off-the-shelf) hardware. The performance results of the software and hardware implementations are shown in Fig. 1. The hardware design running at 90 MHz on the FPGA chip is 25 times faster than fixed-point software running on a 3.0 GHz PC.

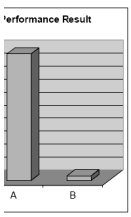


A Software Floating-point ~~ 49s
Fortran code at 3.0GHz PC

B Hardware - WildStar-II Pro
~~ 1.89s
Design working at 90MHz
25X Speedup

3D UPML FDTD algorithm
Model space 50*50*50 cells
Iterate 500 time steps

**3D FDTD Hardware Implementation Performance**

| | Software in FORTRAN | Hardware Design All Cells as Center Cells | Hardware Design All Cell as UPML Boundary Conditions Cells | Hardware Design Combined Center and UPML region Preliminary Test |
|---|---|---|---|---|
| Seconds | 49 | 1.59 | 2.985 | 1.89 |
| MNodes/s | 1.27 | 39.31 | 20.93 | 33.07 |
| Speedup | 1 | 30.9 | 16.5 | 25.9 |

Figure 1: Performance results—softwares vs. FPGA hardware.

There are two Xilinx Virtex-II Pro FPGAs on our FPGA board. In the near future, our research will focus on a dual-FPGA parallel implementation of the FDTD algorithm which is expected to double the speedup.

# Geometric Optics and Electromagnetic Models for Cylindrical Obstacles

**D. Trappeniers, R. G. Gonzàlez, E. van Lil, and A. van de Capelle**
K. U. Leuven, Belgium

**Abstract**—A software prediction tool called EPICS (Enhanced Propagation for Indoor Communications Systems) was developed at the ESAT-TELEMIC division of the K. U. Leuven in two versions: a Geometric Optics (GO) version and a Physical Optics (PO) version. However, like many other three-dimensional package, this can only determine the signal in an environment that can be decomposed into (ir)regular hexahedral obstacles (with 6 sides like rectangular blocks, cubes, etc.) or (complex) combinations of them. Although most of the real life environment can be approximated by these hexahedral obstacles, this might lead to some artefacts like periodic radar cross section variations, the need for multiple diffractions to calculate the signal behind a cylindrical obstacle, or reflections that are ignored (e. g., because the approximated side plane is positioned so that a reflection on that plane can not reach the receiver) is existing. To calculate the signal more accurately for those cases, we need to implement curved obstacles into EPICS. In a first step to achieve this goal, the introduction of cylindrical obstacles is investigated.

In this paper, the general strategy is discussed. The first step is to determine the different intermediate (i. e., penetration, reflection and diffraction) points on the ray between transmitter and receiver. Efficient computational routines have been written and tested for this purpose, mostly solving the problem first in two dimensions (projected in a plane perpendicular to the axis of the cylinder) and then transforming this solution to the three-dimensional problem. Once these intermediate points have been found, one can start with the computation of the electromagnetic field.

In the case of a penetration, the intermediate point(s) can be found very easily (crossing point(s) of a line and a circle) and the electromagnetic computations don't differ from the computations with hexahedral obstacles. For the reflection by a non perfectly conducting surface, the plane wave Fresnel reflection coefficients can be used. Also the finite thickness of the cylindrical walls can be taken into account, using internal (multiple) reflections, if the losses are high or the reflection coefficient of the wall is not to large.

For the diffractions, the two-dimensional geometric problem that needs to be solved to find the diffraction points is the determination of the tangent line to a circle (both from transmitter and receiver). Note that both can have two tangent lines, and one might have to match the two corresponding diffraction points. In this case, the electromagnetic computations for the vertical (i. e., field component parallel with the axis of the cylinder) and horizontal polarisation are done separately. An important issue in these computations is the convergence of the series used for the calculation of the field.

The reflection points on a cylindrical wall can not be found as easily as in the previous two cases. In general, an iterative process is required. This implies that the search for a good starting value is an important issue. Therefore some efficient computer programs were written to find firstly a good starting value of the Newton-Raphson iteration. As for the electromagnetic computations, one has to take into account that the caustics are transformed after the reflections and thus another amplitude factor has to be taken into account.

Although the described routines are not (yet) a part of the EPICS software, new routines based on Geometric Optics (GO) have been written and tested (in matlab) to predict penetration, reflection and diffraction of electromagnetic fields around cylindrical obstacles. This will be used to compute the effects of a curved airport terminal on an Instrument Landing System (ILS).

## 1. Introduction

Most of the real life environment can be approximated by hexahedral obstacles, or combinations of different hexahedral obstacles. Of course this leads to some artefacts like periodic radar cross section variations, the need for multiple diffractions to calculate the signal behind a cylindrical obstacle, or reflections that are ignored, because the approximated side plane is positioned so that a reflection on that plane can not reach the receiver (see Figure 1). To calculate the signal more accurately for those cases, we need to implement cylindrical obstacles into the EPICS program [1].

For each phenomenon, i. e., penetration, diffraction and reflection we briefly discuss the routines to find the intermediate (penetration, diffraction and/or reflection) points [2]. In most cases, this implies that we first solve

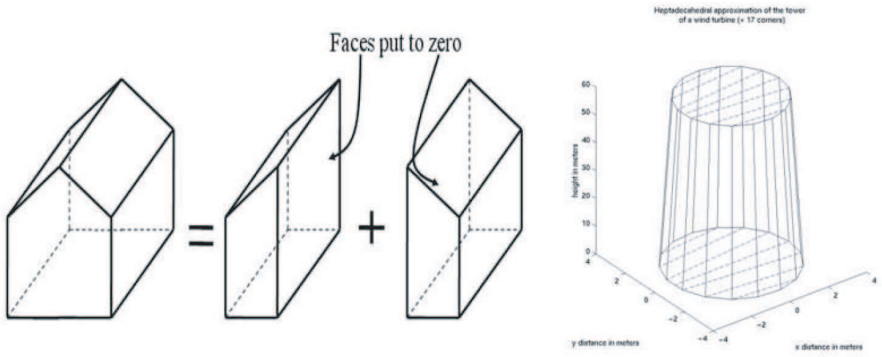


Figure 1: Examples of combinations of hexahedral obstacles to more complex obstacles house (left) and conical tower (right).

a two-dimensional problem which can be easily transformed to the three-dimensional solution. The main part of this paper, however, will be devoted to the electromagnetic computations of the field around these cylindrical obstacles.

## 1. Penetrations and Attenuation

In EPICS the "direct" field between 2 (intermediate) points is calculated in free space. However, this path might be obstructed by an obstacle. Therefore, each wall/obstacle obstructing this path introduces some attenuation of the signal strength. In general we have 3 possibilities: no penetration (e. g., the line transmitter-receiver is parallel to the axis of the cylinder but the distance between the two lines is bigger than the radius), one penetration (if either the transmitter or the receiver is inside the cylinder, while the other is outside, or in the tangent case) or two penetrations (general case).

### 1.1. How to Find the Penetration Points?

The routine to find the penetration points is rather easy: first we determine the crossing points of the line transmitter-receiver (or between 2 intermediate points) with the top and bottom plane of the cylinder. If these points are between the transmitter and receiver, and if the distance of these points to the centre of the top/bottom plane respectively is smaller than the radius of the cylinder, these are valid penetration points. The last step is to investigate the cylindrical wall. Therefore, we need to calculate the crossing points of the line between the projected locations of the transmitter and receiver and a circle. Figure 2 shows the side and top view of some examples (the transmitter is denoted by a $\diamond$, the receiver by a $\circ$ and the penetration point(s) by an $*$).

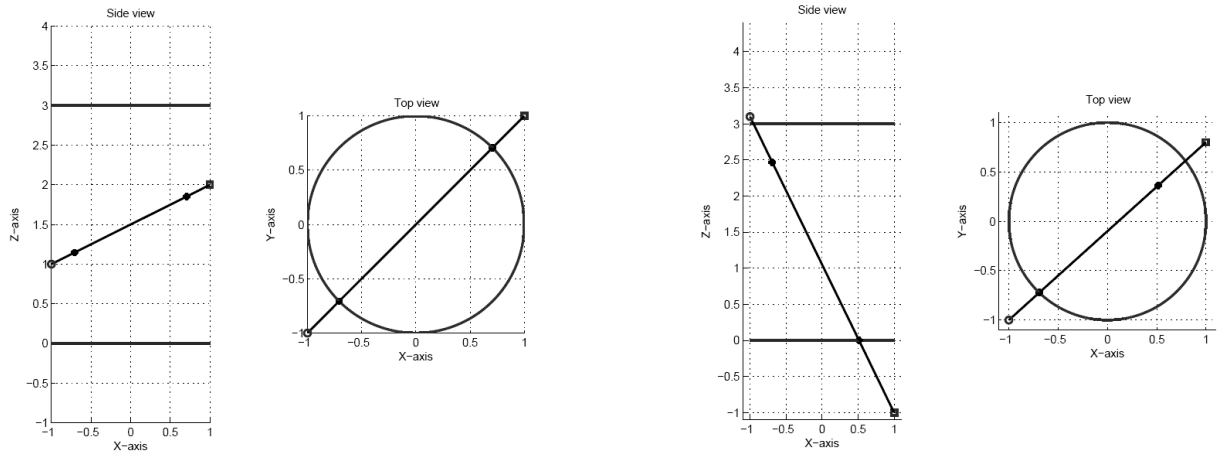


Figure 2: Examples of penetration: both through the side walls (left) and one penetration through a side wall combined with a penetration through the reference/bottom plane (right).

### 1.2. The GO Penetrated Field

Classical Geometrical Optics (GO) states that the high-frequency electromagnetic field propagates along

ray paths, which satisfy the principle of Fermat, which states that the propagation of waves associated with these high frequency fields can be reduced to the study of wave paths along which the travel time is minimal. For perpendicular polarisation, the incident field lies in the plane perpendicular to the plane of incidence (soft boundary conditions). Hard boundary conditions require the incident field to be parallel with the plane of incidence. For the reflection by a non-perfectly electromagnetic conducting surface the plane-wave Fresnel reflection coefficients can be used:

$$\Gamma_{\perp} = \frac{\epsilon' \cos\theta - \sqrt{\epsilon - \sin^2\theta}}{\epsilon' \cos\theta + \sqrt{\epsilon - \sin^2\theta}}$$
$$\Gamma_{\parallel} = \frac{\cos\theta - \sqrt{\epsilon' - \sin^2\theta}}{\cos\theta + \sqrt{\epsilon' - \sin^2\theta}} \tag{1}$$

where $\theta$ is the angle between the incidence ray and the normal of the penetrated plane, $\epsilon$ the permittivity and $\sigma$ the conductivity of the wall. Also the finite thickness of the wall under investigation can be taken into account if the dimensions are small with respect to the distance between transmitter and receiver. In those cases, a plane wave model based on successive reflections within the slab leads to much better results (Figure 3). Only when the losses are small and is not close to 1, edge effects have to be taken into account. However, for practical cases of concrete and thick walls the losses are sufficiently high.

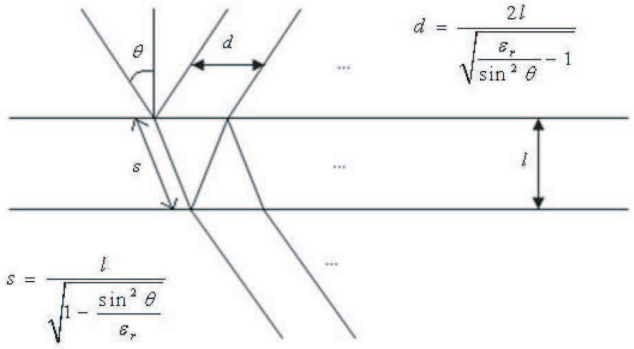


Figure 3: Multiple reflections within a slab.

If we suppose that walls can be approximated by a single slab of dielectric material we can easily see from (Figure 3) that the penetrated field is given by (2), where $\Gamma$ is the appropriate reflection coefficient. Using this equation, the generalised transmission coefficient can be derived (3).

$$\vec{E}^t = \vec{E}^i \sum_{n=1}^{\infty} (1+\Gamma)(-\Gamma)^{2n-2}(1-\Gamma)\, e^{-2(n-1)s\alpha} e^{-2j(n-1)s\beta} e^{j(n-1)k_0 d\sin\theta} \tag{2}$$

$$\tau_g = \frac{\left(1-\Gamma^2\right) e^{-s\alpha} e^{-js\beta}}{\left(1-\Gamma^2\right) e^{-2s\alpha} e^{-j2s\beta} e^{jk_0 d\sin\theta}} \tag{3}$$

where $k_0$ denotes the free space phase constant, while $\alpha$ and $\beta$ are the plane wave attenuation and phase constant of a lossy medium [3], given by (4). As for the case of the generalised reflection coefficient, the penetration coefficient for given material parameters may depend to a great extent on the frequency and thickness used. Inversely, when thickness and frequency are known penetration measurements can be used to estimate the material parameters of different structures [4].

$$\alpha = \omega\sqrt{\frac{\mu\epsilon}{2}}\sqrt{\sqrt{1+\left(\frac{\sigma}{\omega\epsilon}\right)^2} - 1}$$
$$\beta = \omega\sqrt{\frac{\mu\epsilon}{2}}\sqrt{\sqrt{1+\left(\frac{\sigma}{\omega\epsilon}\right)^2} + 1} \tag{4}$$

Figure 4 shows 2 examples of respectively a "perpendicular" incidence, where the line transmitter-receiver is perpendicular to the axis of the cylinder and a "non-perpendicular" incidence. In this last case an extra parameter $m$ can be specified (note that the line transmitter-receiver is still crossing the axis of the cylinder).

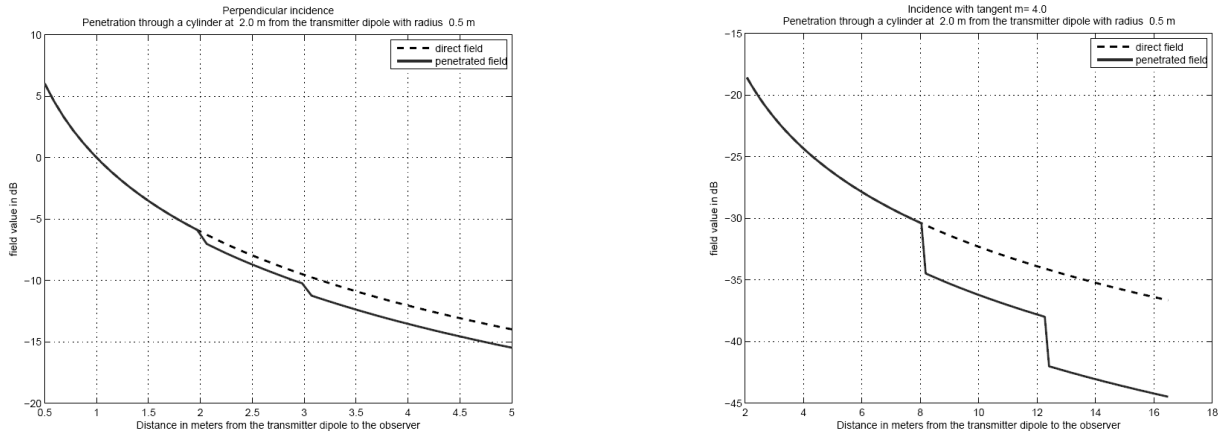


Figure 4: Examples of penetration through a cylinder: perpendicular (left) and non-perpendicular (right) case.

For these examples we used a wall with a thickness $l$ of 0.1 m, a relative permittivity 2.5 ($\epsilon_r$) and a conductivity of 0.036 ($\sigma$). The used frequency was 2.45 GHz.

Note that when $m$ gets very high the losses through the faces are also bigger. For smaller incidence angles, resonance can occur in the wall, so that the losses are not directly proportional with s (see also Figure 3).

## 2. Diffractions

Again we can then solve the geometrical problem (see Figure 5). The determination of the diffraction points in a two-dimensional environment is rather easy: we draw the lines tangent to the circle from both the transmitter and the receiver (see top views). The last step is to determine which of the two points of the transmitter side corresponds with which point at the receiver side (smooth transmission between the air medium and the cylinder surface). Note that we only take diffractions around the cylinder into account. Thus, if one or both of the two diffraction points of one ray turns out to be above the "top" plane or below the "bottom" plane (reference plane), this ray is not taken into account (e. g., Figure 5).

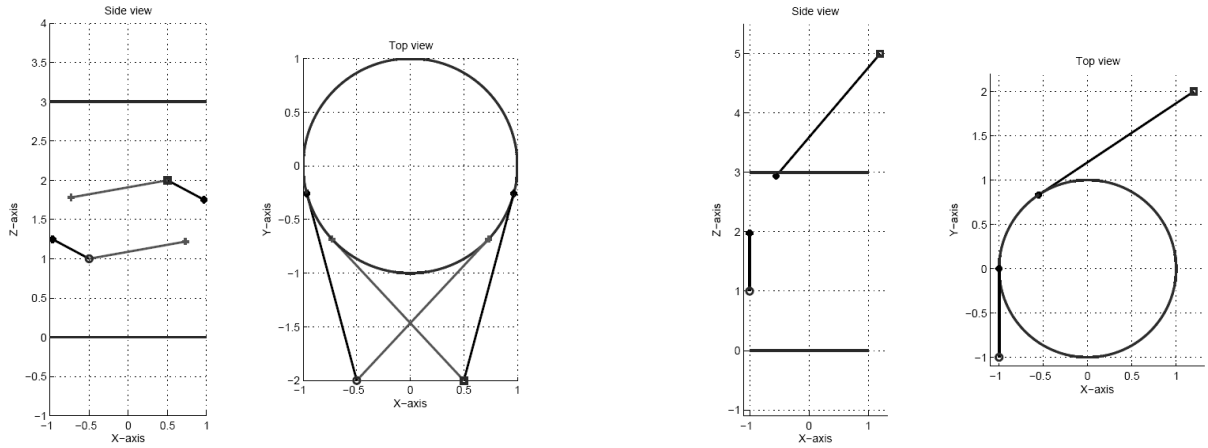


Figure 5: Examples of diffraction: both diffractions are valid (left) and the righter diffraction is ignored (right).

### 2.1. Vertical Polarisation

We have considered a plane wave incident upon a perfectly conducting cylinder (Figure 6). The incident wave is linearly polarised with electric vector $\vec{E}^i$ parallel to the axis of the cylinder. The incident $\vec{k}$-vector is perpendicular to the axis of the cylinder. In terms of cylindrical coordinates, we have

$$\vec{E}^i = \vec{i_z} E_0 e^{jkx} = \vec{i_z} E_0 e^{-jk\rho\cos\theta_0} \tag{5}$$

In this analysis we follow the procedure described by Kong [5].

To match the boundary conditions at $\rho = a$, we transform the plane wave solution into a superposition of cylindrical waves satisfying the Helmholtz wave equation in cylindrical coordinates:

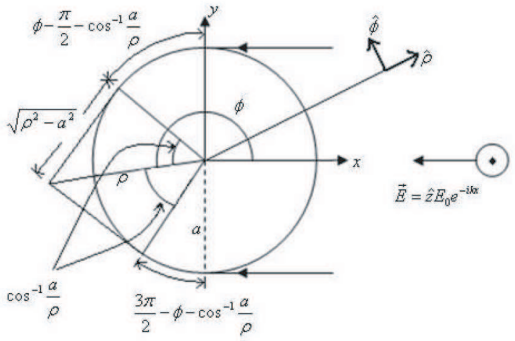


Figure 6: Scattering by a conducting cylinder.

$$e^{-jk\rho cos\theta_0} = \sum_{m=-\infty}^{\infty} a_m J_m(k\rho) e^{jm\phi} \tag{6}$$

The constant $a_m$ can be determined by using orthogonality relations for $e^{jm\phi}$. We multiply both sides by $e^{-jn\phi}$ and integrate over $\phi$ from 0 to $2\pi$. In view of the integral representation for the Bessel function,

$$J_n(k\rho) = \frac{1}{2\pi} \int_0^{2\pi} e^{-jk\rho cos\theta_0 - jn\phi + jn\pi/2} d\phi \tag{7}$$

we obtain $a_m = e^{-jn\pi/2}$ and

$$e^{-jk\rho cos\theta_0} = \sum_{m=-\infty}^{\infty} J_m(k\rho) e^{jm\phi - jm\pi/2} \tag{8}$$

This expression is referred to as the wave transformation, which represents a plane wave in terms of cylindrical waves.

The scattered wave can also be expressed as a superposition of the cylindrical functions satisfying the Helmholtz wave equation. Expecting outgoing waves, we write the solution in terms of Hankel functions of the first kind. The sum of the incident wave and the scattered wave satisfies the boundary condition of a vanishing tangential electric field at $\rho = a$. We find the total solution to be

$$\vec{E} = \vec{i_z} E_0 \sum_{n=-\infty}^{\infty} \left[ J_n(k\rho) - \frac{J_n(ka)}{H_n^{(1)}(ka)} H_n^{(1)}(k\rho) \right] e^{jn\phi - jn\pi/2} \tag{9}$$

The first summation term represents the incident wave; the second summation term, the scattered wave. Note that for $\rho = a$, the field from (9) becomes zero. In the far-field zone, where $k\rho >> 1$, we can make use of the asymptotic formula for $H_n^{(1)}(k\rho)$ and find that the scattered wave takes the form of the first expression of (10) for small radii a, which can be expanded with respect to $ka$.

$$\vec{E_s} \approx \vec{i_z} E_0 \sum_{n=-\infty}^{\infty} \sqrt{\frac{2}{\pi k\rho}} \frac{J_n(ka)}{H_n^{(1)}(ka)} e^{jk\rho + jn(\phi-\pi) - j\pi/4}$$

$$\vec{E_s} = \vec{i_z} j E_0 \sqrt{\frac{2}{\pi k\rho}} \left[ \frac{1}{ln(ka)} + (ka)^2 \cos\phi - \frac{(ka)^4}{8} \cos 2\phi + ... \right] e^{jk\rho - j\pi/4} \tag{10}$$

This series converges rapidly when the radius of the cylinder is small compared with the wavelength, $ka << 1$. The first term is angle-independent and signifies that the scattered wave caused by an infinitely thin wire is isotropic.

### 2.2. Horizontal Polarisation

We have also generalised the procedure and implemented the diffraction by a conducting cylinder for horizontal polarisation. In this case, the electrical field can be expressed like this (see Figure 6):

$$\vec{E^i} = \vec{i_y} E_0 e^{-jk\rho\cos\phi} \tag{11}$$

The scattered wave takes the following form:

$$\vec{E_s} = \vec{i_\rho} \sum_{n=-\infty}^{\infty} a_n H_n^{(1)}(k\rho) e^{jn(n-\pi/2)} + \vec{i_\phi} \sum_{n=-\infty}^{\infty} b_n H_n^{(1)}(k\rho) e^{jn(n-\pi/2)} \tag{12}$$

Once again, we have to require that the $\phi$-component of the total field (incident and scattered field) vanishes for $\rho = a$.

The $\phi$-component of the incident field (11) can be written as:

$$\vec{i}_\phi = -\vec{i_x} \sin\phi + \vec{i_y} \cos\phi$$
$$\vec{E}^i_\phi = -\vec{E_0} e^{-jk\rho\cos\phi} \cos\phi \tag{13}$$

By differentiating Eq. (8) with respect to $\rho$ we obtain:

$$-jke^{jk\rho\cos\phi} = k \sum_{n=-\infty}^{\infty} J'_n(k\rho) e^{-jn(n-\pi/2)} \tag{14}$$

where the derivative of the Bessel function can be found from [6]:

$$J'_n(z) = \frac{J_{n-1}(z) - J_{n+1}(z)}{2} \tag{15}$$
$$J'_0(z) = -J_1(z) \tag{16}$$

When considering only the $\phi$-component of the scattered field (12), we find (17). Indeed, the $\phi$-component vanishes in the far field. This expression can be simplified as we have done above for the vertical polarisation.

$$\vec{E} = \vec{i_\phi} E_0 \sum_{n=-\infty}^{\infty} \left[ J'_n(k\rho) - \frac{J'_n(ka)}{H^{(1)}_n(ka)} H^{(1)}_n(k\rho) \right] e^{jn(\phi-\pi/2)} \tag{17}$$

In Figure 7 both the vertical and horizontal component are shown for 2 examples. Note that the horizontal component gets stronger as the radius of the cylinder increases.

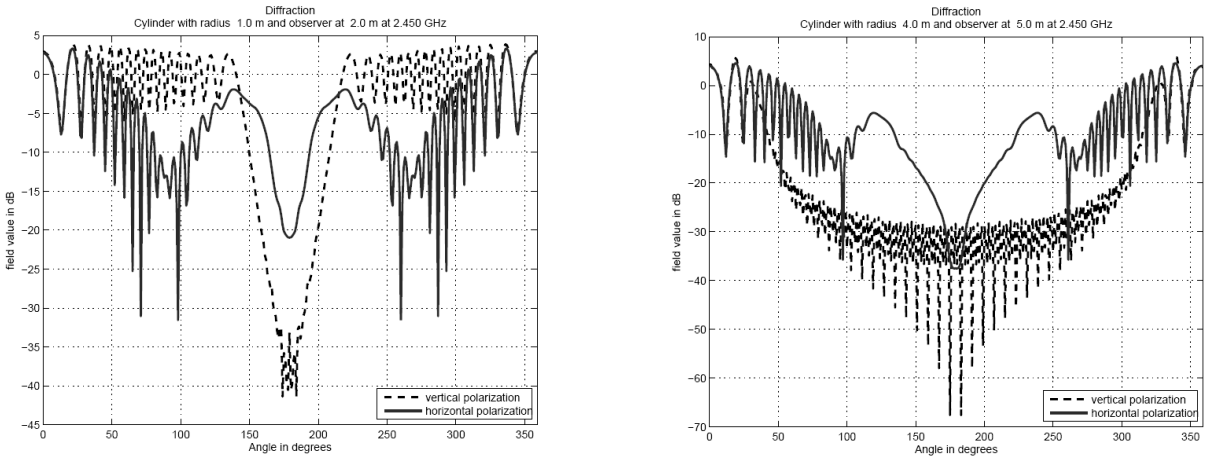


Figure 7: Examples of diffracted fields around a cylinder.

## 3. Reflections

### 3.1. Iterative Process Required to Find the Reflection Points

Whereas for the previous phenomena, the determination of the intermediate points was rather easy, this requires some more attention in the case of a reflection. Of course, one can determine some easy cases as well, e. g., reflections on top/bottom plane, symmetrical cases, etc. The general case for the determination of the reflection point(s), is somewhat more complicated. To find the solutions of the two-dimensional problem we have to solve a fourth degree equation iteratively [2]. This equation is derived by drawing a tangent line on the circle through a chosen reflection point on the circle to determine the mirror images of the transmitter (see Figure 8).

From those points, one can compute the points on the line transmitter-receiver ($\lambda_2$ and $\lambda_2$) where the signal will be reflected to (i. e., the crossing points between this line and the lines from the mirror image of the transmitter and the reflection points under investigation, determined by $\lambda_1$). The goal is to determine $\lambda_1$ so that the vector determined by $\lambda_2$, $\lambda_{2b}$ respectively, is equal to the projection of the receiver. This implies that $\lambda_2$ and $\lambda_{2b}$ should be equal to 1, leading to Eq. (18).

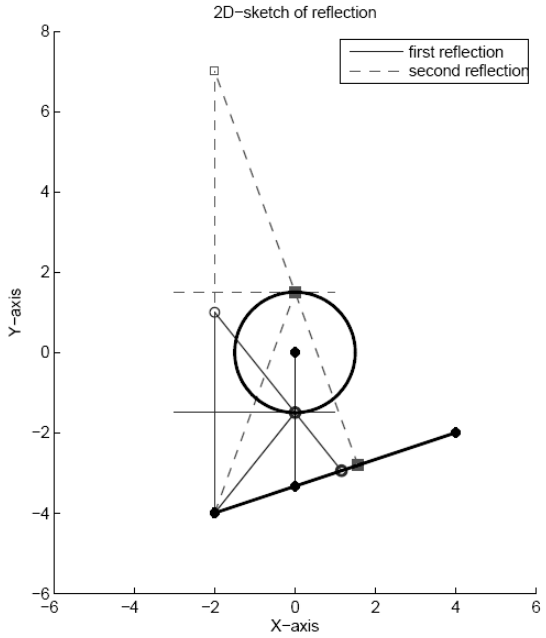


Figure 8: Sketch of general case.

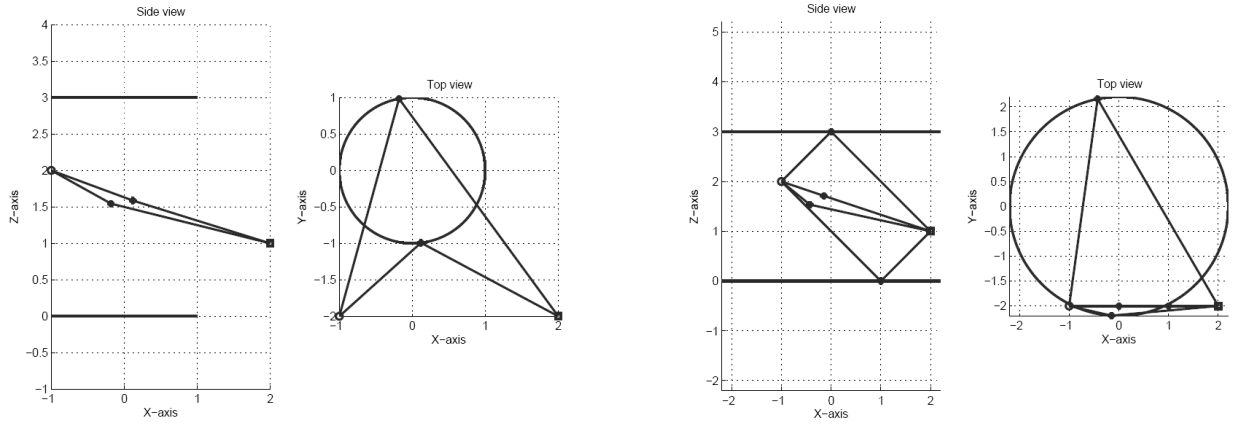


Figure 9: Examples of reflection on a cylinder: without (left) and with (right) reflections on the top and bottom plane.

$$\lambda_{2,2b} = \lambda_1 \left[ \frac{\pm 2R_c\sqrt{a' + b'\lambda_1 + c'\lambda_1^2} - 2a' - b'\lambda_1}{\pm R_c\sqrt{a' + b'\lambda_1 + c'\lambda_1^2} - a' + c'\lambda_1^2} \right]$$
$$\lambda_{2,2b} = 1? \Leftrightarrow A_4\lambda_1^4 + A_3\lambda_1^3 + A_2\lambda_1^2 + A_1\lambda_1 + A_0 = 0 \tag{18}$$

where $a'$ is the quadratic norm of the projected transmitter ($\lambda_1 = 0$), $b'$ twice the scalar product between this vector and the vector between projected transmitter and receiver, $c'$ the quadratic norm of this last vector and Rc the radius of the cylinder.

Unfortunately, we don't always have the possibility to solve a linear equation of the fourth order. Therefore, we will solve this problem iteratively by using the Newton-Raphson method. One can see that equation (18) has 4 possible singularities (nominator equal to zero), and that they are difficult to calculate (start value of Newton-Raphson has to be on the right side of these singularities). Therefore we will search a solution for the inverse function ($1/\lambda_2 = 1$). The last step will be again the transformation of the two-dimensional solution to the three-dimensional solution (excluding reflection points on the cylindrical wall that lie above the top plane or below the bottom plane).

### 3.2. Reflected Field Computations

For the implementation of the computation of the reflected field, one has to keep in mind that after the reflection, the location of the caustics, both for parallel and perpendicular to the axis of the cylinder, might have been changed as is shown in Figure 10.

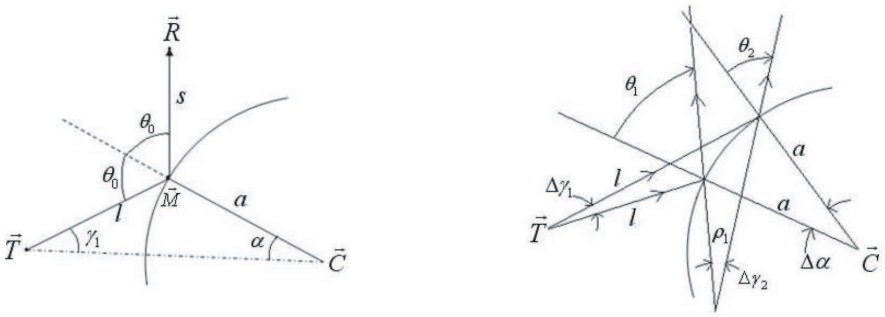


Figure 10: Reflection against a curved surface (parallel case).

Taking a cross-section along one of the radii of curvature, and expressing the arc on the circle as a function of the viewing angles, one can obtain:

$$a\Delta\alpha\cos\theta_0 = l\Delta\gamma_1 = \rho\Delta\gamma_2 \tag{19}$$

where $\Delta\gamma_1 = \Delta\theta_0 - \Delta\alpha$ and $\Delta\gamma_2 = \Delta\theta_0 + \Delta\alpha$. Eliminating $\Delta\alpha/\Delta\theta_0$ this leads to

$$\begin{aligned} \frac{1}{\rho_i} &= \frac{1}{l} + \frac{2}{R_i\cos\theta_0} \\ \frac{1}{R_1} &= \frac{\cos^2\alpha}{a} \\ \frac{1}{R_2} &= \frac{\sin^2\alpha}{a} \end{aligned} \tag{20}$$

where $R_i$ represents the radius of curvature (parallel and perpendicular to the axis). Indeed, it can be shown in analysis that the radius of curvature of a function $y(x)$ is given by:

$$R_i = \frac{y''}{\sqrt{(1+y'^2)^3}} \tag{21}$$

In general the cut of a cylinder is an ellipse which can be expressed by $(x/a')^2 + (y/b')^2 = 1$, where $a' = a$ and $b' = a/\cos\alpha$, bearing in mind that $\alpha$ is the angle between the axis of the cylinder and the cut. Using (21) at the expression of the ellipse, one obtain the formulas of (20). Note that for the parallel case $R_2$ will become infinite. This implies that the distance to the new caustics can be computed:

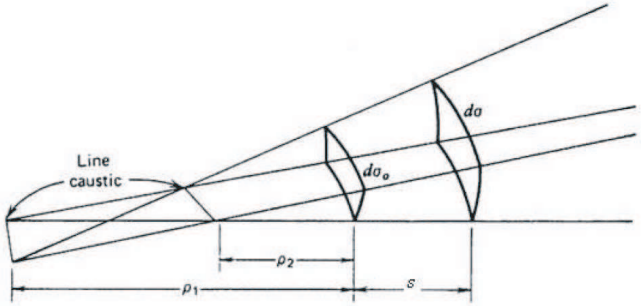


Figure 11: A bunch of rays with a different radius of curvature.

$$\begin{aligned} \frac{1}{\rho_1} &= \frac{1}{l} + \frac{2\cos^2\alpha}{a\cos\theta_0} \\ \frac{1}{\rho_2} &= \frac{1}{l} + \frac{2\sin^2\alpha}{a} \end{aligned} \tag{22}$$

Keeping in mind that the total distance after reflection is given by $d_i = \rho_i + s$, this implies that the field attenuation after reflection can be computed using:

$$|E| = |E_0| \sqrt{\frac{\rho_1 \rho_2}{(\rho_1 + s)(\rho_2 + s)}} \tag{23}$$

where $|E_0|$ is the field at reflection point $\vec{M}$. This attenuation has to be multiplied by the reflection coefficients which can be determined from the slab-approximation of the wall (see Figure 3).

$$\vec{E}^r = \vec{E}^i \left[ \Gamma + \sum_{n=1}^{\infty} (1+\Gamma)(-\Gamma)^{2n-1}(1-\Gamma) e^{-2nsa} e^{-2jns\beta} e^{jnk_0 d \sin\theta} \right] \tag{24}$$

$$\Gamma_g = \Gamma \left[ 1 - \frac{(1-\Gamma^2) e^{-2sa} e^{-j2s\beta} e^{jk_0 d \sin\theta}}{(1-\Gamma^2) e^{-2sa} e^{-j2s\beta} e^{jk_0 d \sin\theta}} \right] \tag{25}$$

### 3.3. Case Study: Brussels Airport Terminal

At Brussels airport, a few years ago a new terminal was build. This A-terminal has a curved shape, to reduce the influence on the Instrument Landing System (ILS) of the neighbouring runway. This ILS systems allows blind landings, and thus has to be very reliable. Using a curved shape, the effect of this new terminal was reduced radically. Figure 12 shows the effect of a rectangular building (left) and a curved building (right) on the differnce pattern of the ILS system (zero along the runway). Note that the buiding was approximated by a cylinder with a horizontal axis, which comes close to the current shape of this A-terminal. One can clearly see that in the zone where reflections can occur (between 3720 and 5200 m along the $x$-axis), the effect of the cylindrically shaped building is much smaller.

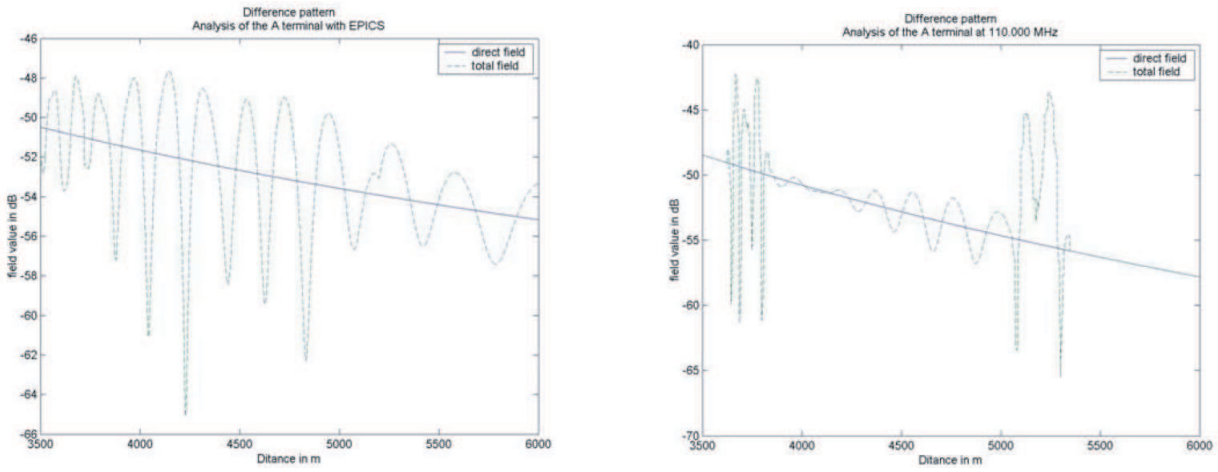


Figure 12: Comparsion between rectangular shaped (left) and curved shaped (right) A-terminal for the difference-pattern of the ILS system.

## 4. Conclusion

In this paper we investigated the influence of a cylindrical obstacle on the electromagnetic signal. Though it is not presented as a part of the EPICS software yet, new routines based on Geometric Optics (GO) have been written and tested to predict penetration, reflection and diffraction of electromagnetic fields around cylindrical obstacles as a step in a future implementation in EPICS.

## Acknowledgement

At the end of this paper, I would like to thank Rubèn Gonzàlez Gonzàlez for the implementation of these routines, during his master thesis.

## REFERENCES

1. De Coster, I., "Deterministic propagation prediction for wireless communication systems," Ph. D. Thesis, K. U. Leuven, Leuven, Belgium, October 2000.

2. Trappeniers, D., E. van Lil, and A. van de Capelle, "UTD-GO implementation for cylindrical obstacles," *COST 273: Towards Mobile Broadband Multimedia Networks*, Paris, France, TD(03)104, May 2003.
3. Inan, U. S. and A. S. Inan, *Electromagnetic Waves*, Prentice Hall, Upper Saddle River, 2000.
4. Bellens, K., "Karakterisering van bouwmaterialen bij breedband communicatiefrequenties," Master thesis, K. U. Leuven, Belgium, May 1999 (Dutch).
5. Kong, J. A., *Electromagnetic Wave Theory*, AMW Publishing, 2000.
6. Abramovitz, M. and C. Stegun, *Handbook of Mathematical Functions with Formulas, Graphs and Mathematical Tables*, AMW Publishing, 2000.

# 3D and 2.5D AGLID EMS Stirring Modeling in the Cylindrical Coordinate System

**G. Q. Xie, J. H. Li, J. Li, and F. Xie**
GL Geophysical Laboratory, USA

**Abstract**—We have proposed the new GL and AGILD modeling and inversion in the PIERS 2005 in Hangzhou. In this paper, we propose 2.5D AGILD modeling algorithm for electromagnetic (EM) stirring, motor and generator design. In the cylindrical coordinate system, the EM field is vector function of $r$, $\theta$, and $z$. The electrical conductivity is only depended on radial coordinate $r$ and vertical coordinate $z$. Upon substituting the Fourier serious of the magnetic field into the strip differential integral equation on boundary strip with pole $\rho = 0$ and Galerkin equation in the internal sub domain, we construct 2.5D AGILD EM stirring modeling in cylindrical coordinate system for the steel and metal continuous casting. There are serious difficulties in the EM stirring modeling by using FEM method and FD method. First, there is $u/\rho^2$ term in the Maxwell magnetic field differential equation in the cylindrical coordinate system, the pole $\rho = 0$ is strong coordinate singularity. The coordinate singularity is difficult in the EM stirring modeling by using FEM and FD method. Our 2.5 AGILDEMS modeling method resolved this difficulty. There is no any coordinate singularity in our 2.5D EM differential integral equation. Second, because the conductivity in air is zero but it is $10^5$ in steel, what is a suitable boundary condition on $\rho = 0$ for current, electric field, and magnetic field that is another difficulty when FEM method and FD method to be used. Our AGILDEMS overcome this difficulty. Based on our 2.5D AGILDEMS algorithm, we developed the 2.5D AGILDEMS modeling software. Many applications show that the 2.5D AGILDEMS software is a powerful tool for design of the EM stirring and real time control monitor in the continuous casting. The AGILD K-$\varepsilon$ flow modeling and software are developing and joining with our AGILD EMS modeling for continuous casting. GL EMS and AGILD EMS modeling can be used for micro, nano motor, generator and geophysics and materials.

## 1. Introduction

In the steel and metal continuous caster, the electromagnetic (EM) stirring (EMS) is an established technique and important approach for improving steel quality. Many EMS with variable style have been working in the steel and metal continuous caster industrial in the world. To exactly calculate the EM field and determine the bloom/billet's size and properties in EMS are an important and difficult task. Because the conductivity in the air environmental is zero but 50,000 1/ohm in steel. The sharp high contrast is difficult in inversion. The EM field artificial boundary condition for infinite domain is inaccurate and complicated. The coordinate singularity is another difficulty in FEM for EMS modeling in the cylindrical coordinate system. The existing EM FEM method and software are not accurate to calculate EM field in EMS. The EMS properties inversion for steel material and conductivity is necessary to develop. We have proposed the new GL and AGILD modeling and inversion in the PIERS 2005 in Hangzhou [1, 2]. We propose the GL method and its advantages for resolving the historical difficulties [3] and the stochastic AGILD EM modeling and inversion in Piers 2006 in Cambridge [4]. In this paper, we propose the 2.5D AGILD EMS stirring modeling using our magnetic field differential integral equation and magnetic field Garlekin equation. Our AGILD EMS modeling is an important tool for EMS design and EMS real time processes monitoring in the continuous caster. Also EMS modeling and inversion are useful for variable motor and generator design, environment, geophysics, coaxial antenna, etc. sciences and engineering.

The description order in this paper is as follows. In the section 2, we derive the 3D and 2.5D magnetic field strip differential integral equations in the cylindrical coordinate system. The 3D and 2.5D magnetic field strip Garlekin equations are derived in the section 3. In the section 4, we present the 3D and 2.5D EMS modeling. The applications of the EMS modeling is described in the section 5. In the section 6, we describe conclusions.

## 2. The 3D and 2.5D Magnetic Field Strip Differential Integral Equations

We derive the 3D and 2.5D magnetic field differential integral equations in the strip domain in the cylindrical coordinate system in this section. We call the equations to be the strip magnetic field differential integral equations.

### 2.1. The 3D Magnetic Field Strip Differential Integral Equation

Upon substituting the field and coordinate transformation between the rectangle and cylindrical coordinate system, we derive the 3D magnetic field strip differential integral equation in the cylindrical coordinate system as follows

$$
\begin{aligned}
&FH3(H,H_{b\rho},H_b^{M_\rho},E_b^{M_\rho})\\
&=H_{b\rho}+\int_\Omega \frac{((\sigma+i\omega\varepsilon)-(\sigma_b+i\omega\varepsilon_b))}{(\sigma+i\omega\varepsilon)}\left(E_{b\rho}^{M_\rho}\Big(\frac{1}{\rho'}\frac{\partial H_z}{\partial\theta}-\frac{\partial H_\theta}{\partial z}\Big)+E_{b\theta}^{M_\rho}\Big(\frac{\partial H_\rho}{\partial z}-\frac{\partial H_z}{\partial\rho'}\Big)+E_{bz}^{M_\rho}\Big(\frac{1}{\rho'}\frac{\partial}{\partial\rho'}(\rho' H)_\theta-\frac{1}{\rho'}\frac{\partial H_\rho}{\partial\theta}\Big)\right)(r')d\rho' d\rho' d\theta dz\\
&+\int_{\partial\Omega-}\frac{1}{(\sigma_b+i\omega\varepsilon_b)}E_b^{M_\rho}\times H\cdot d\vec{S}\\
&-\int_{\partial\Omega-}\frac{1}{(\sigma+i\omega\varepsilon)}\left(\Big(H_{b\theta}^{M_\rho}\Big(\frac{1}{\rho'}\frac{\partial}{\partial\rho'}\rho' H_\theta-\frac{1}{\rho'}\frac{\partial H_\rho}{\partial\theta}\Big)-H_{bz}^{M_\rho}\Big(\frac{\partial H_\rho}{\partial z}-\frac{\partial H_z}{\partial\rho'}\Big)\Big)\rho dz+\Big(H_{b\rho}^{M_\rho}\Big(\frac{\partial H_\rho}{\partial z}-\frac{\partial H_z}{\partial\rho'}\Big)-H_{b\theta}^{M_\rho}\Big(\frac{1}{\rho'}\frac{\partial H_z}{\partial\theta}-\frac{\partial H_\theta}{\partial z}\Big)\Big)\right)\rho' d\rho',
\end{aligned}
\tag{1}
$$

$$
\begin{aligned}
H_\rho(r) &= FH3(H, H_{b\rho}, H_b^{M_\rho}, E_b^{M_\rho}),\\
H_\theta(r) &= FH3(H, H_{b\theta}, H_b^{M_\theta}, E_b^{M_\theta}),\\
H_z(r) &= FH3(H, H_{bz}, H_b^{M_z}, E_b^{M_z}),
\end{aligned}
\tag{2}
$$

where $E$ is the electric field, $H$ is the magnetic field, $E_b^m$ and $H_b^m$ is Green function exciting by the magnetic dipole source, $E_b^m(r',r)$ has weak and integrative singular at $r=r'$, the $r$ locates in the outside boundary of the strip or in the subsurface with $\rho'=0$, the $r'$ locates in $\partial\Omega-$, the internal boundary of the strip, therefore, the 3D strip magnetic field differential integral equation has no coordinate singular at pole $\rho'=0$. It has integrative weak singular kernel.

### 2.2. The 2.5D Magnetic Field Differential Integral Equation

Substituting the EM field Fourier series, $H(\rho,\,\theta,\,z)=\sum_{m=-\omega}^{\infty}H_m(\rho,\,z)e^{im\theta}$, into the 3D strip magnetic field differential integral equation (2), we derive the 2.5D equations in the cylindrical coordinate system

$$
\begin{aligned}
&FH25(H,H_{b\rho},H_b^{M_\rho},E_b^{M_\rho})\\
&=H_{b\rho}+\int_\Omega \frac{((\sigma+i\omega\varepsilon)-(\sigma_b+i\omega\varepsilon_b))}{(\sigma+i\omega\varepsilon)}\left(E_{b\rho}^{M_\rho}\Big(\frac{1}{\rho'}imH_z-\frac{\partial H_\theta}{\partial z}\Big)+E_{b\theta}^{M_\rho}\Big(\frac{\partial H_\rho}{\partial z}-\frac{\partial H_z}{\partial\rho'}\Big)+E_{bz}^{M_\rho}\Big(\frac{1}{\rho'}\frac{\partial}{\partial\rho'}\rho H_\theta-\frac{1}{\rho'}imH\rho\Big)\right)(r')\rho' d\rho' d\theta' dz'\\
&+\int_{\partial\Omega}\frac{1}{(\sigma_b+i\omega\varepsilon_b)}E_b^{M_\rho}\times H\cdot d\vec{S}\\
&-\int_{\partial\Omega}\frac{1}{(\sigma+i\omega\varepsilon)}\left(\Big(H_{b\theta}^{M_\rho}\Big(\frac{1}{\rho'}\frac{\partial}{\partial\rho'}\rho' H_\theta-\frac{1}{\rho'}imH_\rho\Big)-H_{bz}^{M_\rho}\Big(\frac{\partial H_\rho}{\partial z}-\frac{\partial H_z}{\partial\rho'}\Big)\Big)\rho dz+\Big(H_{b\rho}^{M_\rho}\Big(\frac{\partial H_\rho}{\partial z}-\frac{\partial H_z}{\partial\rho'}\Big)-H_{b\theta}^{M_\rho}\Big(\frac{1}{\rho'}imH_z-\frac{\partial H_\theta}{\partial z}\Big)\Big)\right)\rho' d\rho',
\end{aligned}
\tag{3}
$$

$$
\begin{aligned}
H_\rho &= FH25(H,\, H_{b\rho},\, H_b^{M_\rho} E_b^{M_\rho}),\\
H_\theta &= FH25(H,\, H_{b\theta},\, H_b^{M_\theta} E_b^{M_\theta}),\\
H_z &= FH25(H, H_{bz},\, H_b^{M_z} E_b^{M_z}),
\end{aligned}
\tag{4}
$$

## 3. The 3D and 2.5D Magnetic Filed Garlekin Equation

We derive the 3D and 2.5D magnetic field Garlekin equation in the cylindrical coordinate system.

### 3.1. The 3D Magnetic Field Garlekin Equation

Substituting field and coordinate transformation from rectangle to cylinder into the magnetic field Galerkin equation [2], we derive the 3D magnetic field Garlekin equation in the cylindrical coordinate system as follows

$$
\begin{aligned}
&\int_\Omega\frac{1}{\sigma+i\omega\varepsilon}\left(\Big(\frac{\partial H_\rho}{\partial z}-\frac{\partial H_z}{\partial\rho}\Big)\frac{\partial\phi}{\partial z}-\Big(\frac{\partial}{\partial\rho}\rho H_\theta-\frac{\partial H_\rho}{\partial\theta}\Big)\frac{1}{\rho^2}\frac{\partial\phi}{\partial\theta}\right)\rho d\rho d\theta dz+i\omega\int_\Omega\mu H_\rho\phi\rho d\rho d\theta dz=-i\omega\int_\Omega\mu M_\rho\phi\rho d\rho d\theta dz,\\
&\int_\Omega\frac{1}{\sigma+i\omega\varepsilon}\left(-\Big(\frac{1}{\rho}\frac{\partial H_z}{\partial\theta}-\frac{\partial H_\theta}{\partial z}\Big)\frac{\partial\phi}{\partial z}+\Big(\frac{\partial}{\partial\rho}\rho H_\theta-\frac{\partial H_\rho}{\partial\theta}\Big)\frac{1}{\rho^2}\frac{\partial\rho\phi}{\partial\rho}\right)\rho d\rho d\theta d+i\omega\int_\Omega\mu H_\theta\phi\rho d\rho d\theta dz=-i\omega\int_\Omega\mu M_\theta\phi\rho d\rho d\theta dz,\\
&\int_\Omega\frac{1}{\sigma+i\omega\varepsilon}\left(\Big(\frac{1}{\rho}\frac{\partial H_z}{\partial\theta}-\frac{\partial H_\theta}{\partial z}\Big)\frac{1}{\rho}\frac{\partial\phi}{\partial\theta}-\frac{\partial\phi}{\partial\rho}\Big(\frac{\partial H_\rho}{\partial z}-\frac{\partial H_z}{\partial\rho}\Big)\right)\rho d\rho d\theta dz+i\omega\int_\Omega\mu H_z\phi\rho d\rho d\theta dz=-i\omega\int_\Omega\mu M_z\phi\rho d\rho d\theta dz,
\end{aligned}
\tag{5}
$$

### 3.2. The 2.5D Magnetic Field Garlekin Equation

Upon substituting the Fourier series, $H(\rho,\,\theta,\,z)=\sum_{m=-\omega}^{\infty}H_m(\rho,\,z)e^{im\theta}$ into the 3D Garlekin equation (5), we derive the 2.5D magnetic field Garlekin equation in the cylindrical coordinate system as follows

$$\begin{aligned}
&\int_{\Omega}\frac{1}{\sigma+i\omega\varepsilon}\left(\left(\frac{\partial H_\rho}{\partial z}-\frac{\partial H_z}{\partial \rho}\right)\frac{\partial \phi}{\partial z}-\left(\frac{\partial}{\partial \rho}\rho H_\theta-imH_\rho\right)\frac{1}{\rho^2}im\phi\right)\rho d\rho dz+i\omega\int_{\Omega}\mu H_\rho\phi\rho d\rho dz=-i\omega\int_{\Omega}\mu M_\rho\phi\rho d\rho dz,\\
&\int_{\Omega}\frac{1}{\sigma+i\omega\varepsilon}\left(-\left(\frac{1}{\rho}imH_z-\frac{\partial H_\theta}{\partial z}\right)\frac{\partial \phi}{\partial z}+\left(\frac{\partial}{\partial \rho}\rho H_\theta-imH_\rho\right)\frac{1}{\rho^2}\frac{\partial \rho\phi}{\partial \rho}\right)\rho d\rho dz+i\omega\int_{\Omega}\mu H_\theta\phi\rho d\rho dz=-i\omega\int_{\Omega}\mu M_\theta\phi\rho d\rho dz,\\
&\int_{\Omega}\frac{1}{\sigma+i\omega\varepsilon}\left(\left(\frac{1}{\rho}imH_z-\frac{\partial H_\theta}{\partial z}\right)\frac{1}{\rho}im\phi-\frac{\partial \phi}{\partial \rho}\left(\frac{\partial H_\rho}{\partial z}-\frac{\partial H_z}{\partial \rho}\right)\right)\rho d\rho dz+i\omega\int_{\Omega}\mu H_z\phi\rho d\rho dz=-i\omega\int_{\Omega}\mu M_z\phi\rho d\rho dz,
\end{aligned}\tag{6}$$

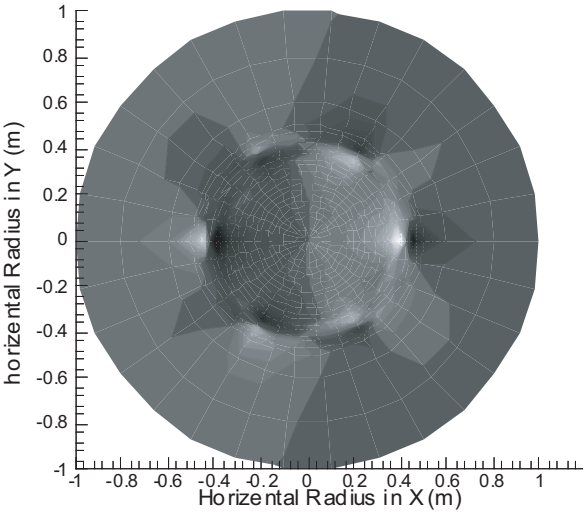


Figure 1: Rotation magnetic field $H_\theta$ in time =0 s.

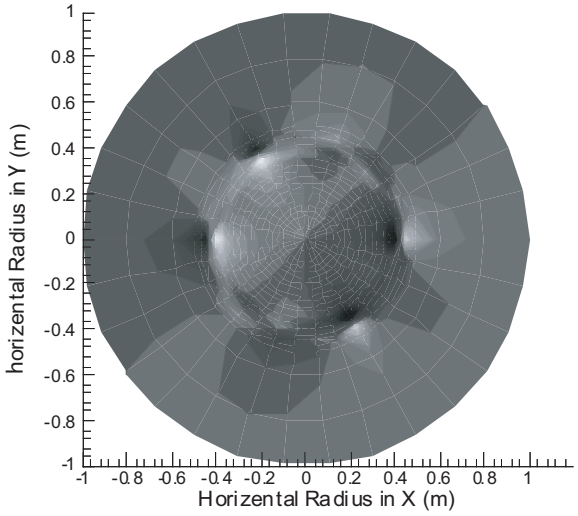


Figure 2: Rotation magnetic field $H_\theta$ in time =0.1 s.

## 4. 3D and 2.5 D EMS Modeling

### 4.1. 3D EMS Modeling

We use collocation FEM the 3D strip magnetic field differential integral equation (2) in the boundary strip domain including pole point $\rho=0$, and the 3D magnetic field Galerkin equation (5) in the reminder internal domain without pole $\rho=0$ to construct 3D AGILD EMS magnetic field modeling for EM field in the Stirring and motor etc industrial engineering and sciences.

### 4.2. 2.5D EMS Modeling

We use collocation FEM the 2.5D strip magnetic field differential integral equation (4) in the boundary strip domain including pole point $\rho=0$, and use the 2.5D magnetic field Galerkin equation (6) in the reminder internal domain without pole $\rho=0$ to construct 2.5D AGILD EMS magnetic field modeling for EM field in the stirring and motor etc industrial engineering and sciences.

## 5. The Applications of the AGILD EMS Modeling

Our 3D and 2.5D AGILD and GL EMS modeling has been used to calculate the EM field for several EM stirring with variable style. Some asynchronous EMS stirring is designed as follows: its outer radius is 500 mm, the internal radius is 350 mm, and it is divided 6 sectors. The electric current has inverse direction for any adjoining two sectors. The input electric current density intensity is 1 A/mm$^2$. The frequency is 4 Hz. Before installation of the stirring without steel flow, the factor did measure the magnetic field intensity. By using digit magnetic GAUSS meter, the measurement value of the magnetic field intensity at center of the stirring is 1500 Gauss. By using our 2.5D AGILD EMS modeling simulation, the evaluated magnetic field intensity is 1513.28 Gauss at center of the stirring. The rotational EM field is very accurate and very stable. The AGILD EMS

rotation magnetic field in caster $H\rho(\rho, \theta, zc, t)$ at the 0.0∼0.25 second are plotted in the Figures 1 and 4. They show that by using the GL EMS and AGILD EMS modeling, the rotational magnetic field's frequency is exactly 4 Hz. The GL EMS [3, 5] and 2.5D AGILD EMS magnetic field $H_\rho$, $H_\theta$ intensity are plotted in Figures 5 and 6, the red curve is the GL magnetic field and blue curve is AGILD magnetic field, the two curves are close matched. GL EMS and AGILD EMS modeling can be used for micro, nano motor, generator and group holes geophysics and materials etc. We are developing GL and AGILD K-$\varepsilon$ model steel flow driving by the EMS Lorentz force and join it with AGILD EMS modeling to work for the steel and metal continuous casters.

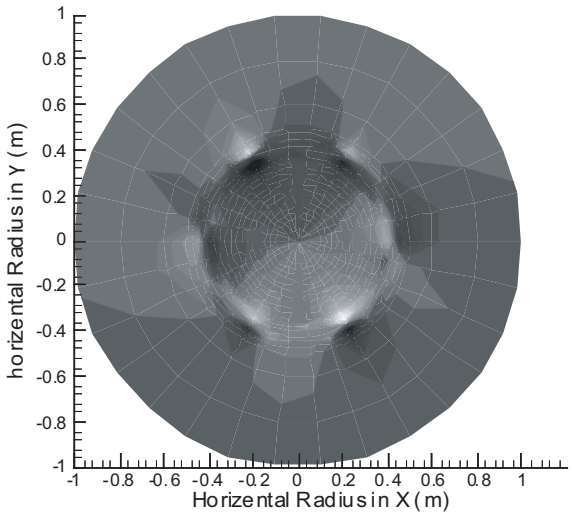


Figure 3: Rotation magnetic field $H_\theta$ in time =0.2 s.

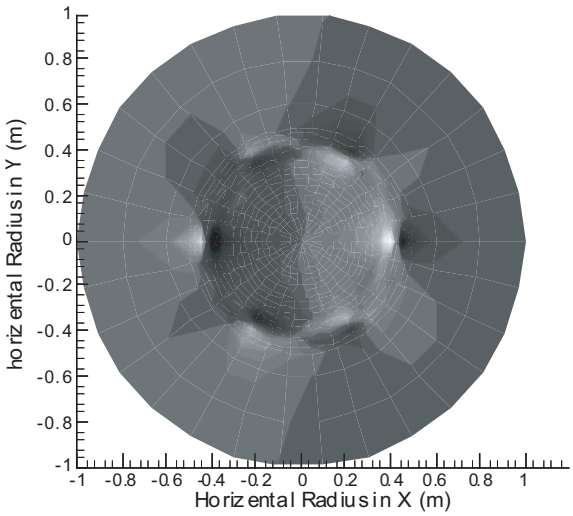


Figure 4: Rotation magnetic field $H_\theta$ in time =0.25 s.

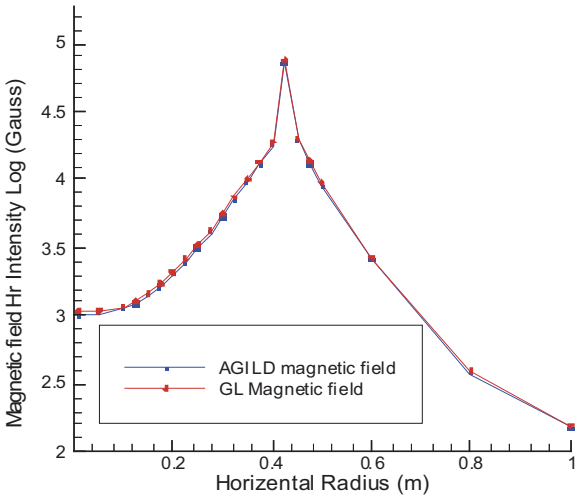


Figure 5: The magnetic field $H_\rho$ intensity ,The red line is GL magnetic field, The blue line is AGILD magnetic field.

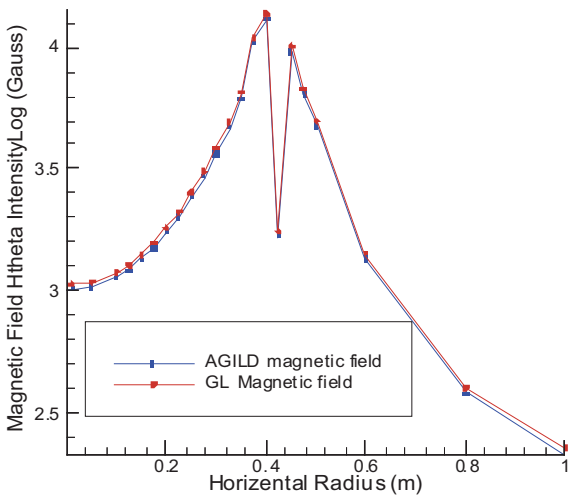


Figure 6: The magnetic field $H_\theta$ intensity, The red line is GL magnetic field, The blue line is AGILD magnetic field.

## 6. Conclusions

Many EM field in the stirring and motor simulations show that the 3D and 2.5D AGILD, and GL EMS modeling are accurate and fast and stable. The AGILD EMS has merits over existing FEM, FD, and Born approximation. The 3D and 2.5D AGILD and GL EMS modeling will be new tools for widely applications in the sciences and engineering.

**REFERENCES**


1. Xie, G., J. Li, and F. Xie, "New global and local electromagnetic field (GL) modeling and inversion," *proceeding of PIERS2005 in Hangzhou*, 68, 2005.
2. Xie, G., J. Li, and F. Xie, "Advanced GILD EM modeling and inversion," *Proc. PIERS*, Hangzhou, 105.
3. Xie, G., F. Xie, and J. Li, "New GL method and its advantages for resolving historical difficulties," to be presented in PIERS 2006 in Cambridge of USA, 2006.
4. Li, J., G. Xie, and F. Xie, "New stochastic AGLID EM modeling and inversion," to be presented in PIERS 2006 in Cambridge of USA, 2006.
5. Xie, G., J. Li, and F. Xie, "2.5D AGLID EM modeling and inversion," to be presented in PIERS 2006 in Cambridge of USA, 2005.
6. Xie, G., F. Xie, and J. Li, "New GL and GILD superconductor electromagnetic modeling," *Proceeding of PIERS2005 in Hangzhou*, 187, 2005.
7. Li, J., G. Xie, and F. Xie, "AGILD K-$\varepsilon$ flow modeling," Report of GLGEO, GLP05006. Its copyright and patent belong to the authors in GL Geophysical Laboratory, 2005.
8. Xie, G., F. Xie, and J. Li, "GL EM modeling and inversion based on the new EM integral equation," Report of GLGEO, GLP05001, GLGEO has copyright and patent for the GL method, 2005.
9. Xie, G., J. Li, and J. Li, "New AGILD EMS EM field modeling," *PIERS 2005 in Hangzhuo*, 179, 2005,
10. Li, J., G. Xie, and Z. Liao, "Electromagnetic stirring using GL electromagnetic field," *Proceeding of PIERS2005 in Hangzhou*, 180, 2005.

# Time-domain Source-model Technique Analysis of Two-dimensional Electromagnetic Scattering Problems

**A. Ludwig and Y. Leviatan**
Technion - Israel Institute of Technology, Israel

Time-domain integral equation solvers for analyzing transient scattering phenomena continue to be a subject of considerable interest in the computational electromagnetics community. In this paper, we study a somewhat different time-domain integral-equation solution. Instead of using a standard surface formulation, we present a mesh-free formulation for the solution of the electromagnetic scattering problem of a two-dimensional metallic cylinder illuminated by a TM (transverse magnetic) plane wave pulse. In the proposed solution, we adapt the frequency-domain source model technique, which has been found to be efficient and versatile computational tool for analysis of time-harmonic wave scattering problems, to allow direct time-domain analysis of transient scattering problems. In this solution, the scatterer is replaced with a discrete set of spatially impulsive filamentary sources, each carrying longitudinally-uniform but time-dependent electric currents that are subsequently expanded in terms of pulse functions of yet-to-be-determined amplitudes. The filamentary sources are located on a mathematical surface interior to the cylinder surface. They are assumed to radiate in an unbounded free-space and their fields, which are known analytically, span the transient scattered field in the region exterior to the cylinder. The source amplitudes are determined by requiring that the boundary condition for the total tangential electric field be satisfied at a suitably chosen set of time instances and at a selected set of testing points on the boundary of the cylinder. The effect of solution method parameters, such as the spatial density and temporal discretization of the fictitious sources, on the accuracy and stability of the results is studied. A spatio-temporal discretization criterion for an explicit formulation of the time-domain source-model solution is presented to allow the use of a simple marching-on-in-time algorithm. The modification of this algorithm to treat an implicit formulation of the time-domain source-model solution is discussed, and the advantages of such a formulation are outlined. Finally, the use of a combined-source formulation and its effect on the resulting stability is studied.

# New 2.5D/3D AGILD Geophysical EM Multiple Cross Holes' Imaging

**J. Li**[1], **M. Oristaglio**[2], **F. Xie**[1], **and G. Xie**[1]

[1]GL Geophysical Laboratory, USA
[2]Schlumberger-Doll Research, USA

Seismic wave, acoustic wave and electromagnetic (EM) field inversion are used for geophysical subsurface imaging. Because there is electric conductivity in the Earth underground, the diffusion EM field with infinite velocity causes the EM inversion more ill posed than seismic and acoustic inversion. The optimizing data configuration, suitable frequency band, and vanishing boundary error, translating coordinate singularity in forward modeling, and combining strong regularizing and weak regularizing etc. approaches will be benefit for EM inversion. In this paper, we propose a "new 2.5D/3D AGILD geophysical EM multiple cross holes' imaging" algorithm. We choose the three, four, and five cross holes data configuration. Based on the AGILD EM modeling and inversion in Piers 2005 in Hangzhou [1] and 3D and 2.5D AGILD EMS modeling in the cylindrical system in Piers 2006 in Cambridge [2], we present the 3D EM modeling and multiple 2D conductivity inversion using the multiple cross holes data. In existing 2.5D algorithm, the conductivity and EM parameters are supposed to be independent on the variable $\theta$ and only 2D inversion is processed. Therefore, the existing 2.5 D algorithm can only make rough imaging for whole cylinder subsurface. By using a variable weight average strategy, our new 2.5D inversion can be used to do multiple 2D conductivity inversions using the multiple cross holes data. In the other hand, there is strong coordinate singularity $1/\rho^2$ at $\rho = 0$ in exiting FD and FEM EM modeling in the cylindrical coordinate that is a historical difficulty. Our 2.5D AGILD geophysical EM multiple cross holes' imaging algorithms overcome this difficulty because the strip magnetic field differential integral equation has no coordinate singularity at $\rho = 0$. We use 3D strip magnetic field differential integral equation in the boundary pole strip domain with pole $\rho = 0$ and use magnetic field Garlekin equation in the remainder domain to construct 3D AGILD magnetic and EM field modeling to obtain the model data. Using statistics geology average strategy, we make the 2, 3, 4, or 5 multiple cross holes' 2D AGILD EM inversions. Our new AGILD multiple cross holes' imaging will be useful for geophysical exploration, oil exploration, Earthquake exploration, geophysical engineering, environment characteristic monitoring, nondestructive testing, medical imaging, and material and nano sciences etc sciences and engineering.

**REFERENCES**

1. Li, J. and G. Xie, "A cubic-hole finite element for 3D resistivity modeling," "Three-dimensional electromagnetics," edited by Michael Oristaglio, *Geophysical Developments*, No. 7, 591–599, 2000.
2. Li, J., G. Xie, and F. Xie, "New stochastic AGLID EM modeling and inversion," to be presented in *PIERS 2006 in Cambridge of USA*, 2005.
3. Xie, G., J. Li, and F. Xie, "New global and local electromagnetic field (GL) modeling and inversion," *proceeding of PIERS2005 in Hangzhou*, 68, 2005.
4. Xie, G., J. Li, and F. Xie, "Advanced GILD EM modeling and inversion," *Proc. PIERS*, Hangzhou, 105.
5. Xie, G., F. Xie, and J. Li, "New GL method and its advantages for resolving historical difficulties," to be presented in *PIERS 2006 in Cambridge of USA*, 2006.
6. Xie, G., J. Li, and F. Xie, "2.5D AGLID EM modeling and inversion," to be presented in *PIERS 2006 in Cambridge of USA*, 2006.
7. Xie, G., F. Xie, and J. Li, "New GL and GILD superconductor electromagnetic modeling," *Proceeding of PIERS2005 in Hangzhou*, 187, 2005.